UNIVERSIDADE DA BEIRA INTERIOR
Engenharia

Automatic Annotation of Cellular Data

João Neves

Dissertação para obtenção do Grau de Mestre em
Engenharia Informática
(2º ciclo de estudos)

Orientador: Prof. Doutor Hugo Proença

Covilhã, Junho de 2013

Acknowledgements

During this year, several persons have contributed in different ways to the development of this work. To each one I will leave a thank you note.
Firstly, I would to thank to my supervisor Hugo Proença, whose expertise, understanding, and patience improved my graduate experience and paved the way to my success. I am also grateful to him for the trust placed in me to take part of CellNote project, where this thesis has been developed.
A word of thanks is due also to my colleagues in CellNote project, especially Bruno for the help and support provided during the time spent in Oporto.
I am also grateful to the biologists Helena Castro and Tânia Cruz, whose advices were crucial while developing this work.
To my parents Carlos and Fernanda, sister Joana I would like to express my gratitude for encouragement and support.
To my girlfriend Marisa, I am thankful for her help, love and support over all this year.
Last, but not least I would like to acknowledge my friends whose friendship was very important to me during this time.

Resumo alargado

A anotação de células é uma tarefa comum a diversas áreas da investigação biomédica. Normalmente, esta tarefa é realizada de forma manual, sendo um processo demorado, cansativo e propício a erros. Neste trabalho, focamos o nosso interesse na anotação de imagens de fluorescência com infeções de *Leishmania*, que representa um destes casos. *Leishmania* são parasitas unicelulares que infectam mamíferos, sendo responsáveis por um conjunto de doenças conhecidas por leishmanioses. *Leishmania* usam vertebrados como hospedeiros residindo dentro dos seus macrófagos. Por conseguinte, um modelo adequado para o estudo destes parasitas é infectar *in vitro* culturas de macrófagos. A capacidade de sobrevivência/replicação da *Leishmania* nessas condições artificiais pode então ser avaliada por parâmetros, como, por exemplo, a percentagem de macrófagos infectados, o número médio de parasitas por macrófagos infectados e o índice de infeção. Essas métricas são geralmente determinadas pela contagem de parasitas e macrófagos ao microscópio. Ambos os tipos de células podem ser facilmente distinguidos com base no seu tamanho e cor, resultante de diferentes afinidades de corantes fluorescentes. A passagem desta tarefa do microscópio para o computador já foi conseguida através de aplicações como o CellNote, contudo, apesar de mais fácil e interativa, a anotação continua a ser manual. A evolução da abordagem manual para um processo automático representa um passo natural e lógico, constituindo o principal objetivo deste trabalho. Para isto iniciámos a investigação pela revisão dos principais métodos de deteção e contagem celular. As características das imagens com infeções de *Leishmania* impossibilitam a utilização dos métodos estudados, de tal modo que optámos por desenvolver uma nova abordagem, capaz de lidar com as várias especificidades destas imagens. Também durante o processo de revisão de literatura analisámos os dois métodos previamente propostos para realizar a anotação automática de infeções de *Leishmania*. Estes revelaram um desempenho abaixo do requerido pelos parasitologistas, justificando também o desenvolvimento de uma nova abordagem. Durante a concepção do sistema investigámos diversas técnicas de deteção celular, onde a deteção de *blobs* se destacou pelos resultados positivos. Para segmentar as regiões citoplasmáticas optámos pela utilização de algoritmos de *clustering*. Estes não foram capazes de solucionar casos em que existia sobreposição de estruturas celulares, motivando assim o método de separação desenvolvido. Este método baseia-se maioritariamente na análise de contorno, sendo as suas concavidades geradoras de separação entre citoplasmas. Através da combinação destas fases foi possível detetar macrófagos e parasitas com mais precisão. Para confirmar esta conclusão testámos não só a nossa abordagem mas também as duas abordagens previamente desenvolvidas para este problema. Os desempenhos alcançados evidenciam não só uma melhoria comparativamente às restantes abordagens como também mostram que a nossa abordagem assegura resultados satisfatórios comparativamente aos obtidos manualmente. Em suma, o trabalho desenvolvido produziu um sistema capaz de realizar a anotação automática de imagens de fluorescência com infeções de *Leishmania*, tendo originado um artigo aceite para publicação na conferência *International Conference on Image Analysis and Recognition* (ICIAR) 2013.

Abstract

Life scientists often need to count cells in microscopy images, which is very tedious and a time consuming task. Henceforth, automatic approaches can be a solution to this problem. Several works have been devised for this issue, but the majority of these approaches degrade their performance in case of cell overlapping. In this dissertation we propose a method to determine the position of macrophages and parasites in fluorescence images of *Leishmania*-infected macrophages. The proposed strategy is mainly based on blob detection, clustering and separation using concave regions of the cells' contour. By carrying out a comparison with other approaches that also addressed this type of images, we concluded that the proposed methodology achieves better performance in the automatic annotation of *Leishmania* infections.

Keywords

Cell detection, cell counting, blob detection, cell clustering, concave points

Contents

List of Figures

List of Tables

Lista de Acrónimos

UBI	Universidade da Beira Interior
DNA	Deoxyribonucleic acid
RNA	Ribonucleic acid
DAPI	4',6-diamidino-2-phenylindole
AHE	Adaptive Histogram Equalization
ROI	Region Of Interest
DoG	Difference of Gaussians
LoG	Laplacian of Gaussian
SVM	Support Vector Machine
GMM	Gaussian Mixture Model
FN	False Negative
FP	False Positive
IBMC	*Instituto de Biologia Molecular e Celular*
ICIAR	International Conference on Image Analysis and Recognition
#M	Number of Macrophages
#P	Number of Parasites
#IM	Number of Infected Macrophages
PI	Percentage of Infection
NPI	Mean Number of Parasites per Infected Macrophage
IX	Infection Index

Chapter 1

Introduction

Microscopes have long been used to allow life scientists observe cellular organisms. The scales achieved by these devices enable the analysis of cellular organisms properties. Many experiments aim to inspect the effects of certain drugs or treatments, therefore microscope is used as a way to observe such effects. In many cases this observation requires the counting, delimiting or measuring areas of interest of cellular organisms, as exemplified by figure 1.1. However, these tasks require life scientists intervention and are sometimes hard to perform while observing the image through microscope lens. With the possibility to record the microscope images digitally, life scientists improved the way to perform these tasks, mainly if platforms as CellNote [Lop10] are used. CellNote enables the graphical annotation of microscope imagery, i.e. identify the locations of cellular organisms with graphical marks. Annotation provides a more interactive and easy way of count cellular organisms, reduces the time consumed and increases the accuracy in such tasks. Despite everything, annotation is still manual and requires life scientists attention and time.

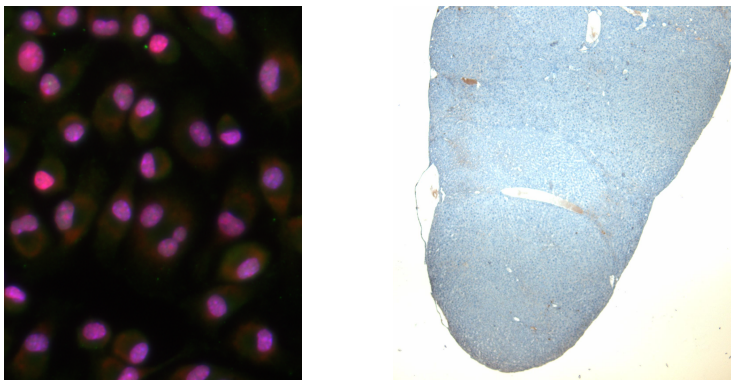

(a) (b)

Figure 1.1: Common tasks performed in microscope images. Left figure presents an image where cell counting is required. Right figure presents an image where blue areas need to be segmented and their area measured.

The advent of affordable and high-performance computers boosted the development of pattern recognition and digital image processing techniques, which paved the way for the emergence of methods able to replicate human skills. Microscope image processing arises as the combination between the pattern recognition and digital image processing techniques applied to microscope imagery. Pattern recognition concerns about the classification of data based on the analysis of patterns, whereas digital image processing provides techniques to enhance certain patterns. Combined, these areas can devise methods to automatically analyse microscope images and extract relevant information from them. As a result, manual tasks carried out by life scientists can be delegated to computers with the help of Microscope image processing techniques. Even though these approaches are not error free, they can be considered reliable when high performances are achieved.

1.1 Motivation and Objectives

In this work we are particularly interested in fluorescence images with *Leishmania*-infected macrophages. Cellular organisms comprised in these experiments are macrophages and leishmaniasis parasites, whereas the common goal is to determine infections levels. To infer these levels, life scientists need to count the number of macrophages and parasites, together with the number of macrophages infected by parasites. Such tasks are highly boring and time-consuming, that can not be neglected either, since they are crucial to determine infection levels and draw experiment conclusions.

Microscope image processing can be a solution to automatically annotate *Leishmania* infections. We aim to develop a method able to determine macrophages and parasites locations, as well as their association, i.e which parasites are infecting a macrophage. Several tracking methods have been proposed to deal with microscope images, notwithstanding they can not be directly applied to *Leishmania* infections, since the characteristics of cellular data are not the same. Heretofore only two approaches addressed the annotation of *Leishmania* infections. As before stated, in no case an automatic approach is error free, nevertheless their performances were not high enough to be considered reliable by life scientists. Therefore, our main objective is to develop a method robust to the variations existing in these type of cellular organisms. For that purpose, several cell tracking methods will be analysed and their main ideas gathered and tested in *Leishmania* data.

1.2 Thesis Outline

The remainder of this thesis is organized as follows: chapter 2 gives a short summary of fluorescence microscopy, as well as the methodology used by life scientists to guide their experiments. Moreover, we present the different type of information comprised in images with *Leishmania* infections and the statistical measures that life scientists aim to infer from these images. A collection of digital image processing techniques and Pattern Recognition methods commonly used in cellular image processing are also presented in the second chapter, together with the most relevant works in the scope of cell tracking. Chapter 3 describes in detail all the phases of the proposed method. In the chapter 4 the main advantages and drawbacks are highlighted and compared with similar approaches. Furthermore, an optimization strategy is presented, together with a comparison between the results achieved by our approach and others that addressed the same problem. Finally, conclusions are drawn in chapter 5 and the future work is outlined.

Chapter 2

State of Art

This chapter starts with a short description of the fluorescence microscopy foundations, along with a brief introduction to how parasitologists establish a experiment. Following this general introduction, we focus in *Leishmania*. The information contained in the type of images this work aims to analyse and the statistical measures longed by parasitologists are also described. Then, we describe the pattern recognition and digital image processing techniques, commonly used to analyse microscopy images, emphasizing those used in fluorescence microscopy images.

2.1 Fluorescence Microscopy

The fluorescence microscopy technique has its roots mainly in the property that certain molecules have to absorb radiation with high energy, ultraviolet and x-rays, and emit radiation in the visible spectrum. Molecules with this property can be classified as fluorescence or phosphorescence, depending on how the emission lasts. In both cases the absorption of high energetic radiation results in the movement of the outer electrons to higher energy levels, normally called excitation levels. In the fluorescence molecules, called fluorophores, these levels are very unstable and the electrons return quickly to the fundamental levels after the absorption, whereas in the phosphorescence molecules this process takes a longer time. These differences result in distinct durations per emissions of visible light, this is, fluorescence molecules only emit visible light when a source of excitation is present, whereas the phosphorescence molecules continue to emit even after the source of excitation is turned off. The fluorophores can be natural or synthetic, however in fluorescence microscopy the commonly-used fluorophores are synthetic as these are specially modified to emit light in a tight wavelength and to bind to specific components of cells[Lak06]. The main reason and advantage behind the fluorescence microscopy is the possibility to visually differentiate different structures in the image using different colors.

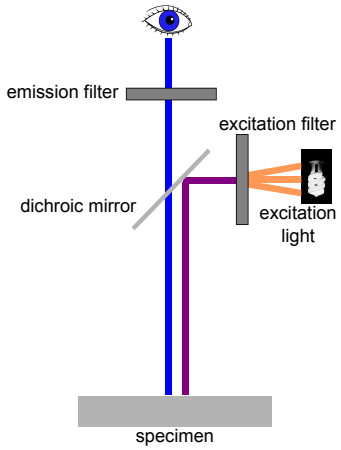

Figure 2.1: Fundamental schema of a fluorescence microscope

This visual separation is achieved using different fluorophores that emit visible light with different

wavelengths, what in practice labels structures with different colors. Figure 2.1 illustrates the schematic view of a fluorescence microscope. In fluorescence microscopy a light source is combined with a filter in order to provide the excitatory radiation with the right wavelength. This radiation is reflected to the specimen using the dichroic mirror. The specimen should contain the fluorophores that will be excited and emit radiation at a different wavelength. The radiation emitted is normally visible and is first filtered before reach the eye of the observer. An example that illustrates such technique is the stain of the nucleus using 4',6-diamidino-2-phenylindole (DAPI) [Kap95], that highlights the Deoxyribonucleic acid (DNA) of the cell.

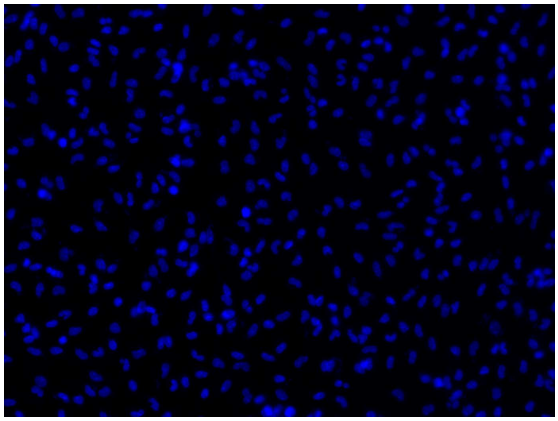

Figure 2.2: Example of specimen treated with DAPI.

When a specimen, previously stained with this molecule, is submitted to excitation, the ultraviolet light passes through because DAPI is excited by radiation with a maximum wavelength of 358 nm. After the absorption, the fluorophore will emit visible light, while the remaining specimen will only reflect ultraviolet, that is not detected by the observer. With this, cell nuclei is highlighted and clearly distinguishable, as shown in figure 2.2.

2.1.1 Steps of an experiment

In the normal activity of a researcher there are questions whose answer requires the use of fluorescence microscopy, as for example the test of drugs against parasites [CSS+02]. In order to determine if a drug has any effect in a given population of parasites, cultures of cells are infected according with the experiment requirements. After this, the researcher isolates a few samples that will remain without that drug, designated as control samples. The other samples are used to test the effect of different concentrations of the drug. Each test is performed in triplicate, therefore sets of 3 samples are treated with a certain concentration of the drug, and thus, there will be as many sets as the number of concentrations tested. Figure 2.3 illustrates a routine experiment in which three different concentrations of a drug were tested. After the experiment is finished, the cells are stained with specific fluorescent probes to identify the mammalian host cell and the parasites by fluorescence microscopy. In the microscope, the researcher acquires images from each sample and as only a small region of the sample can be observed at the time, the researcher has to screen different areas, taking 6 to 10 pictures of disjoint regions of the sample. Figure 2.4 exemplifies a sample from where 6 images were taken using the fluorescence microscope. Each one of these images has to be manually counted by the researcher in order to infer the indexes of infection.

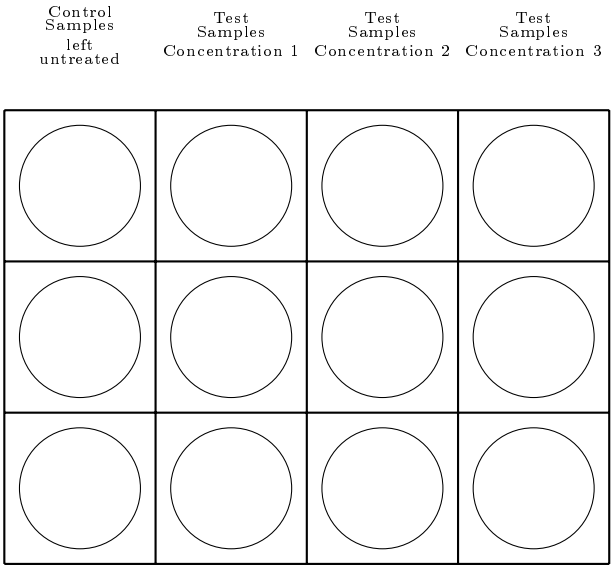

Figure 2.3: Example of the samples used by the parasitologists to test the effect of a drug.

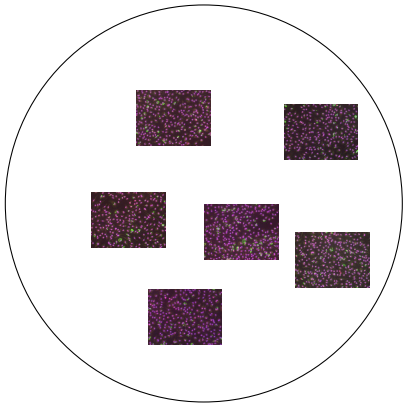

Figure 2.4: Cover slip containing a sample and the locations of the images collected using the fluroescence microscope .

2.1.2 *Leishmania*

In this work the parasite under study is *Leishmania*. This parasite lives inside mammalian cells and is responsible for a disease designated leishmaniasis. The life cycle of these parasites is divided between a insect host and a mammalian vertebrate. The sandflies are the insect host of *Leishmania*, when these feed from the blood of a vertebrate the parasite can be transmitted to the bloodstream. Once in the vertebrate, the parasite gains access and invades specific cells where it starts reproducing itself, leading eventually to the rupture of the host cell. The released parasites can now invade more cells in the mammalian organism resulting in the damage of organs such as the spleen and the liver and eventually, leading to death of the infected patient.

2.1.3 Image Properties

In this work the used microscope images were all fluorescent and used to test *Leishmania* infections. As mentioned before, the advantage of using fluorescent images is the visual separation between different molecular structures. The images infected with the Leishmaniasis parasite comprise two organisms, the macrophages and the parasites. Figure 2.5 shows an example where the nucleus and cytoplasm of the macrophages and the entire body of the parasites are visible.

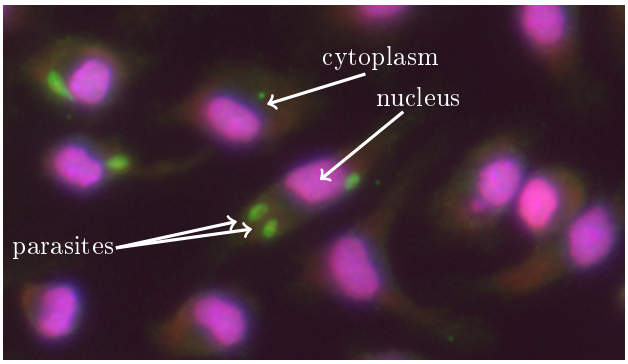

Figure 2.5: Part of a fluorescence image and the structures contained.

The visual differentiation, responsible for the distinction between the macrophages and the Leishmaniasis parasites in an image, is achieved using specific fluorophores. In this case two or three fluorophores are used, depending on the parasitologists needs. The fluorphore used to mark green the body of parasites is Alexa Fluor® 488. In order to mark as red the nuclei of the macrophages it is used the Propidium iodide. As it binds mainly to the DNA structure of the organisms, and the DNA is located in the nucleus is easy to conclude why the macrophages nucleus have the largest red components in the image. Propidium iodide is mainly used to mark as red the macrophages nucleus, but is important to note that the nucleus of parasites are also marked as red due to the DNA present in the nuclei of the parasites. However, as they are much smaller than the nuclei of macrophages their visibility is not always ensured. Another property of Propidium Iodide is that it binds not only to DNA but also to Ribonucleic acid (RNA). This explains why the cytoplasm of macrophages, that contains RNA, can be seen as red shades. The last fluorphore used is DAPI, that is not always used as it adds redundant information to the previously extracted. This fluorphore binds to DNA too, but by contrast it does not bind to RNA.
In this work the used images were acquired with microscopes of Carl Zeiss company [Zei13] that records the images digitally in a proprietary format known as zvi. This file contains not only the intensities of red, green and blue channels but also informations related to the acquisition conditions.

2.1.4 Objectives of a experiment

Once the sample images are collected, the biological researcher needs to determine the infection levels in the conditions tested. Based on these results they can understand the effect of a drug and extract the experiment conclusions. The measures that the parasitologists consider important in the testing of the effect of drugs in *Leishmania* infections are the Percentage of Infection (PI), the mean Number of Parasites per Infected cell (NPI) and the Infection indeX (IX). PI is defined as

$$PI = \frac{\sum_{i=1}^{N} C(i)}{N}, \quad (2.1)$$

where $C(i)$ is an indicator function equal to 1 if the i^{th} macrophage is infected and 0 otherwise. N is the number of macrophages in the image. NPI is defined as

$$NPI = \frac{\sum_{i=1}^{N} P(i)}{\sum_{i=1}^{N} C(i)}, \quad (2.2)$$

where $P(i)$ is the number of parasites infecting the i^{th} macrophage. IX is defined as

$$IX = PI * NPI = \frac{\sum_{i=1}^{N} P(i)}{N}, \quad (2.3)$$

These measures can only be determined by counting the number of macrophages and parasites present in the image. In order to determine $P(i)$ the associations between macrophages and parasites have to be manually performed too. Parasitologists use the cytoplasm to accomplish the association. A parasite must be associated with a macrophage if it is located in the cytoplasm of the macrophage. Initially, this process was carried out while observing the images at the microscope, but nowadays parasitologists can afford a more comfortable option. CellNote [Lop10] is a software platform especially developed to display the images obtained at the microscope and provide an interactive way to graphically annotate an image. CellNote has reduced the time that parasitologists spend counting an image and increased the reliability of the process, being a great help for this duty. Despite this, the process is still manual, what is very tedious and time consuming. A solution to this problem is to use image analysis techniques and build a computer vision system to automatically annotate the images.

2.2 Methods used in Cellular Image Processing

The field of Image Processing and Computer Vision has been evolving dramatically with the constant development of new techniques. This improves not only the number of techniques available but also their quality and reliability. In this scope, the cellular image analysis is one sub-field that has experienced some advantages with this growth. Most of the methods that have been recently proposed aim at automatically acquire images as well as extract information from them. Although each approach is usually specific to a type of cell or problem, it tends to follow the main structure of a Computer Vision system. This structure is given in the figure 2.6.

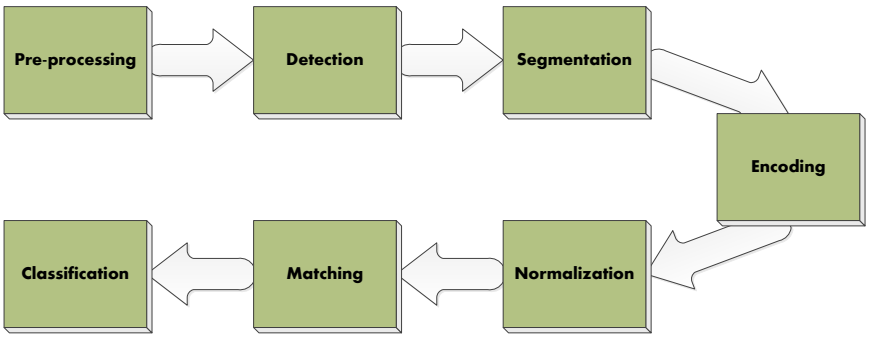

Figure 2.6: Schema of the main phases of a Computer Vision system.

In this section the methods used in cellular image processing are summarized, organized with respect to the phases of a Computer Vision system.

2.2.1 Pre-processing

In the majority of the cases the input of a Computer Vision system is not noise-free. In this case the input are images and issues with the resolution, acquisition conditions and protocol are very

usual. In order to achieve a solution the first approach is usually to remove noise from the image, what is done in the pre-processing phase.

2.2.1.1 Gaussian Filter

A Gaussian filter is used to remove the high frequencies of a signal, which represent the detail. This detail is often meaningless to the analysis of the image. This filter is parametrized by equation 2.4 and is often used with $\sigma_x = \sigma_y = \sigma$ and $u_x = u_y = 0$. Under these restrictions a set of filters only differ in the value given to σ. The value of σ controls the level of detail removed from the image. Higher values of σ yield a filter close to a uniform distribution, as it can be seen in the difference between the gaussians filters in the figures 2.7a and 2.7b. Besides that, higher values of σ will cause a more blurred image, with less detail.

$$G(x, y; \sigma) = \frac{e^{-(\frac{(x-u_x)^2}{2\sigma_x^2} + \frac{(y-u_y)^2}{2\sigma_y^2})}}{2\pi\sigma_x\sigma_y} \quad (2.4)$$

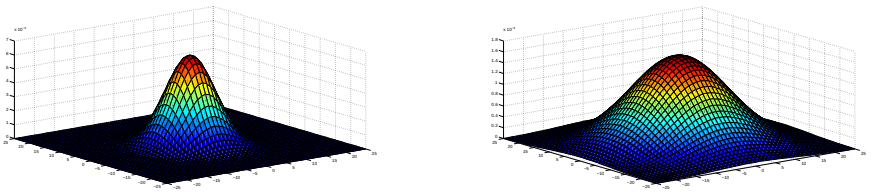

(a) $\sigma = 5$ (b) $\sigma = 10$

Figure 2.7: Gaussian Filters

2.2.1.2 Contrast Stretching

The computational representation of images is a function of pixel intensities that are constrained to a range of values. Due to poor acquisition conditions, sometimes images only use a part of the available range. A consequence of this can be seen in the figure 2.8a where the contrast is so low that is very hard to distinguish the cells from background. It can be confirmed by the image histogram, presented in the figure 2.8b, that the majority of the intensity values are constrained to a small range. This problem is very common in our interest data: the figure 2.8a belongs to the raw dataset used in this work. The aim of contrast stretching technique is to expand the values in the image to the whole range of intensities available. If the whole range available is used the intensity values will be less closer to each other and increasing the contrast and making more clear the boundaries between objects, as it can be seen in the figure 2.9a.

2.2.1.3 Histogram Equalization

As it was explained in the last subsection, the histogram of an image enables to perceive the problems that an image suffers due to poor conditions acquisition. This way, a popular method of enhancing an image is equalizing its histogram. The aim of histogram equalization is transform the image I into a image E in such way that histogram of E is uniform. In order to carry out this transformation it is needed a function $q = T(p)$ that assigns a new intensity value q to each intensity value of I, represented by p. E is the result of image $T(I)$, i.e. each pixel with intensity

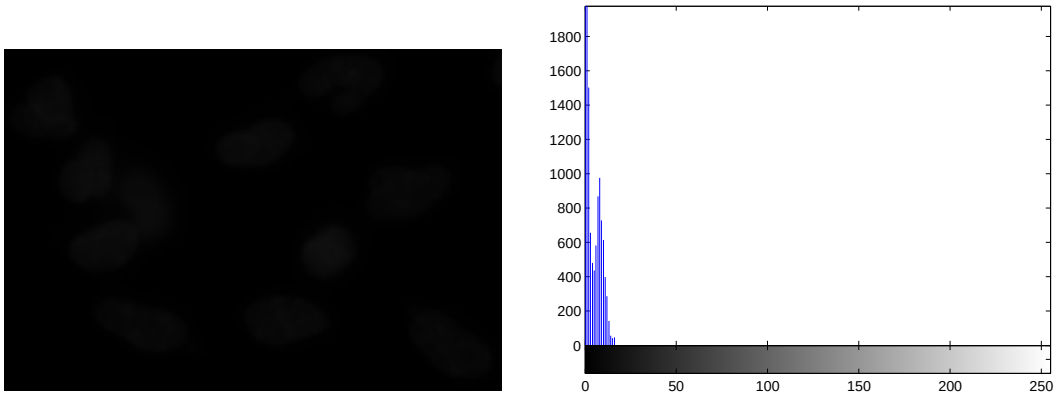

(a) (b)

Figure 2.8: Small portion of a sample as it was acquired(left). The histogram of the image(right).

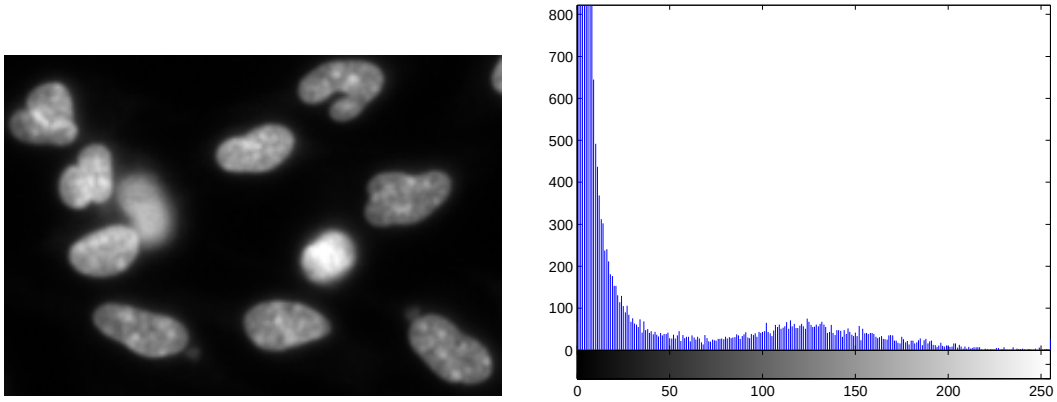

(a) (b)

Figure 2.9: Result of contrast stretching technique applied to figure 2.8a(left). The histogram of the resulting image (right).

p be replaced with the intensity q. The derivation of the function T is now explained in the continuous space and it is only there that the histogram of the image E is completely uniform. [GW01]

First let H_I and H_E represent the histograms of I and E respectively. It can be seen that

$$\int_{q_0}^{q} H_E(t)\,\mathrm{d}t = \int_{p_0}^{p} H_I(t)\,\mathrm{d}t \qquad ,q \in [q_0, q_d], p \in [p_0, p_d] \quad (2.5)$$

where q_0 and q_d are the minimum and the maximum intensity values that q can take. As the aim is to ensure that H_E is uniform it is easily derived that $H_E(a) = H_E(b) \forall a, b$. What leads to

$$H_E(q) = \frac{M \times N}{q_d - q_0} \iff \int_{q_0}^{q} H_E(t) = \frac{M \times N}{q_d - q_0}.(q - q_0), \quad (2.6)$$

where M and N represent the width and height of the images. Joining this result with equation 2.5 it is obtained

$$\frac{M \times N}{q_d - q_0}.(q - q_0) = \int_{p_0}^{p} H_I(t)\,\mathrm{d}t, \quad (2.7)$$

From the equation 2.7 it can be seen each q can be obtained from p the following way

$$q = \frac{\int_{p_0}^{p} H_I(t)\,\mathrm{d}t}{M \times N}.(q_d - q_0) + q_0, \quad (2.8)$$

In equation 2.8 it has been defined $T(p)$ in a continuous space, so it can now be defined the function T in the discrete space.

$$T(p) = \frac{\sum_{i=p_0}^{p} H_I(i)}{M \times N}.(q_d - q_0) + q_0, \quad (2.9)$$

As stated before, q_0 and q_d are the minimum and maximum intensity values desired for the output image. If a 8-bit grey-scale is desired, q_0 and q_d would be 0 and 255. In the figure 2.10a it can be seen the result of histogram equalization technique applied to figure 2.8a. The differences between the histograms can be seen by comparing figures 2.8b and 2.10b. A consequence of a more uniform histogram is a more balanced image in the gray levels. This can be seen in the figure 2.10a where the darker gray levels were transformed into brighter values. Besides that, it can be seen that the more predominant gray levels are now more distant in the gray scale than the less predominant. This is another consequence of obtaining a more balanced histogram and explains the contrast enhancement of figure 2.10a.

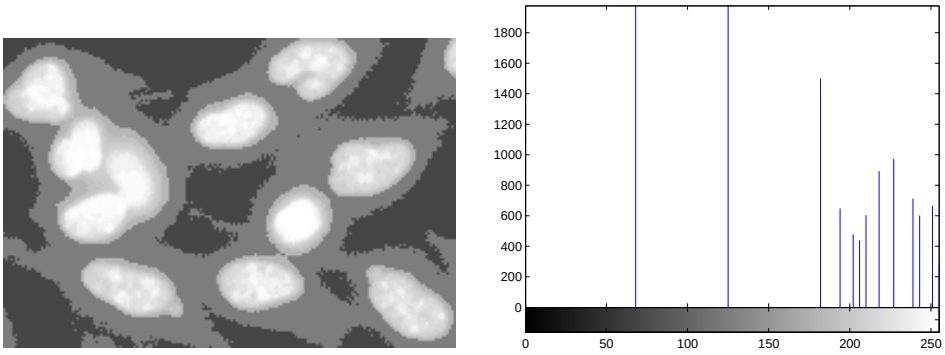

(a) (b)

Figure 2.10: Result of the histogram equalization technique applied to figure 2.8a (left). The histogram of the resulting image (right).

2.2.1.4 Adaptive Histogram Equalization(AHE)

The AHE [KLW76, PAA+87] is an improvement of the histogram equalization and aims to overcome the shortcomings of histogram equalization in images where the gray level is highly uncertain in subregions of the image. As explained before, the histogram equalization technique uses a transformation function that maps each intensity to another. This can be insufficient to enhance the contrast of some regions because this transformation depends of global intensities but not depends of the spatial location of the pixels. The AHE technique solves this problem using only a neighbourhood of the pixel to define the transformation function. To do this it is necessary to obtain

a transformation function to each pixel, and apply a histogram equalization to the neighbourhood of the pixel. To avoid the computational burden of this technique a speed up improvement is used based on interpolation. By comparing figures 2.10a and 2.11a it can be seen the differences between the histogram equalization and the AHE. The original image, figure 2.8a, has a very uniform distribution with reduced variations in intensity, what explains the result of AHE. As each neighbourhood has intensity levels very low and close to the central pixel, its intensity will not increase as much as it has increased in figure 2.10a.

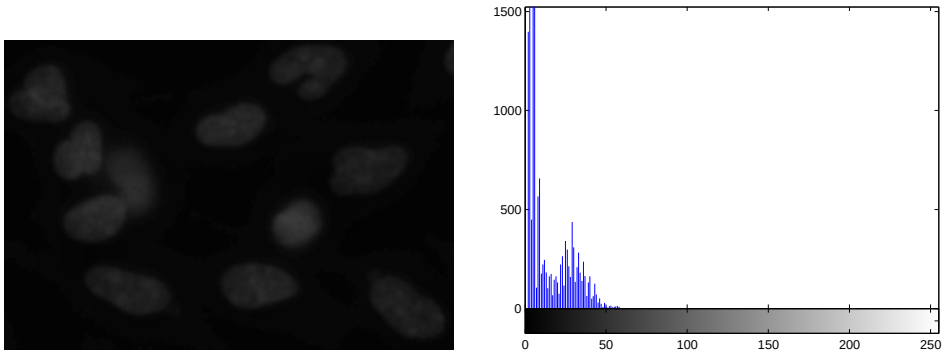

(a) (b)

Figure 2.11: Result of AHE technique applied to figure 2.8a(left). The histogram of the resulting image (right).

2.2.1.5 Morphological Operators

Mathematical morphology is a technique based on set theory that is very popular in image processing[Ser83, Soi03]. The morphological operators are used to transform a image. Initially, the mathematical morphology could only be applied to binary images but later it was extended to gray scale images. Each operator is associated with a structuring element that controls how the morphological operator transforms the image. The main operators are erosion and dilation, defined as $I \ominus S$ and $I \oplus S$ respectively, where I is the image and S the structuring element. The morphological operations are processed using the structuring element to sweep the image pixel by pixel. In each pixel the structuring element is centered and the intersection between the structuring element and the image in that region is found. The result of the intersection determines the value of the pixel in the transformed image. Erosion yields 1 only if the intersection is equal to the structuring element, while in the case of the dilation it is 0 only if the intersection is empty. In figure 2.12 it can be seen the result of erosion and dilation in figure 2.12c and 2.12d respectively, when applied to a simple rhombus.

2.2.2 Detection

After enhance the quality of the images or highlight some of their interesting points with pre-processing techniques, the next phase is usually the detection of regions of interest (ROI). The aim is to find regions that may contain the objects of interest. These regions are usually rectangles and do not need to frame the object exactly, constituting only an estimation of where is more likely that the object is. The purpose of detection is discard unimportant regions of the image and keep only the most promising ones. This way, it helps the segmentation to be accurate and less time consuming.

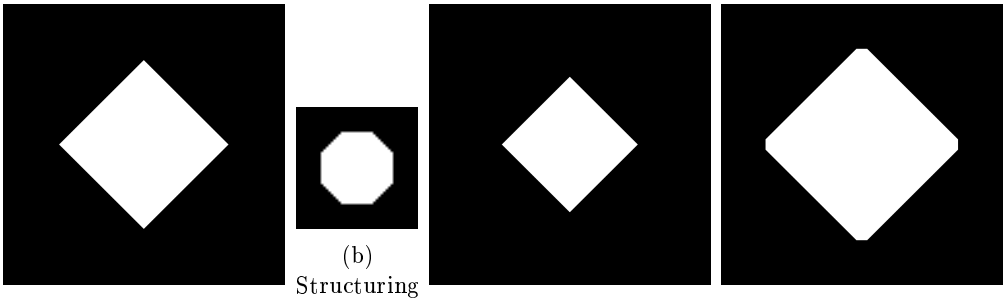

(a) Original Image (b) Structuring Element (c) Eroded image (d) Dilated image

Figure 2.12: Erosion and dilation applied to a rhombus.

2.2.2.1 Otsu's Method

This method was originally proposed by Otsu [Nob79] and is very common in image processing[FS88]. This method is threshold-based but it is more robust than a simple fixed threshold, because it uses the information of the histogram of the image to find the best threshold value. The method foundation is the idea that if an image has two main classes, the background and the foreground, then its histogram would mainly present two distributions. In other words, the histogram is expected to be bimodal, and the best gray level k that separates the two classes is the value of k that minimizes the within class variance $\sigma_W^2(k)$ defined as the weighted sum of the variance of each class:

$$\sigma_W^2(k) = \omega_1(k)\sigma_1^2(k) + \omega_2(k)\sigma_2^2(k), \quad (2.10)$$

where

$$\omega_1(k) = \sum_{i=0}^{k} p(i) \quad (2.11a)$$

$$\omega_2(k) = 1 - \omega_1(k). \quad (2.11b)$$

The result of this method applied to figure 2.9a can be seen in figure 2.13. As it can be seen, it perfectly separates the cells from the background, and the bi-modality of the histogram is also evident.

Figure 2.13: Result of Otsu's method applied to figure 2.9a.

2.2.2.2 Edge Detection

One of the most important features of an image is the edges of the objects it contains. The edges allow to recognize a object by its frontiers. In the image processing filed they are very important and used mainly to feed the segmentation phase, as they give an estimate of the contour of a object. The main idea behind the process to find the edges in an image is that the edges are regions with a higher change of gray level intensity than other regions in the image. The best way to evaluate the amount of variation of a signal is its derivative so the basis of almost every edge detection method is the extreme values of the derivative of the image. The derivative operations are usually obtained using filters that approximate the derivative by the convolution between an image and the filter. In figure 2.14 the Prewitt filters [Pre70] are illustrated , used to approximate the derivative of an image. Figure 2.15a illustrates the gradient of the derivative of image 2.9a using the Prewitt filters. The edges can be obtained after using a threshold on the gradient image. In order to solve the problem of the choice of the threshold level some methods were proposed [Can86, Har84].

$$\begin{bmatrix} -1 & 0 & 1 \\ -1 & 0 & 1 \\ -1 & 0 & 1 \end{bmatrix} \begin{bmatrix} -1 & -1 & -1 \\ 0 & 0 & 0 \\ 1 & 1 & 1 \end{bmatrix}$$

Figure 2.14: Two filters of Prewitt used to approximate the derivatives of a image in horizontal and vertical direction.

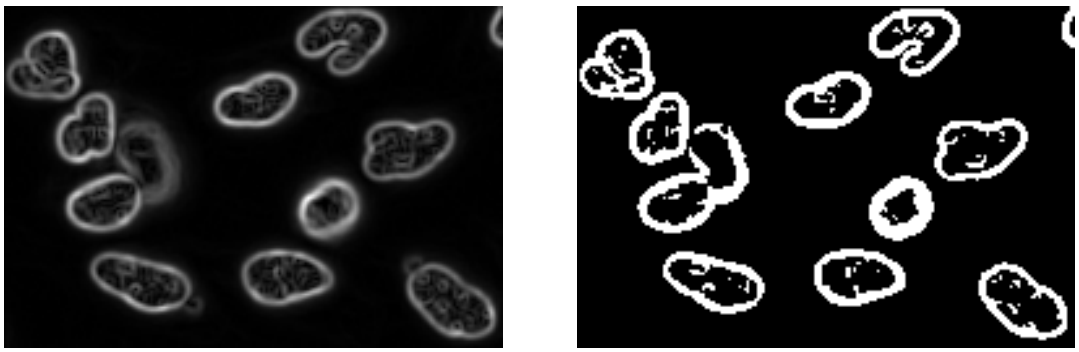

(a) Gradient of the derivative of figure 2.9a using the Prewitt Filters.

(b) Edges of the original image, figure 2.9a, using a threshold on the gradient image.

Figure 2.15

2.2.2.3 Laplacian

As discussed before, the edge detectors use the high values of the magnitude of the first order partial derivatives of the image to find edges. The main problem of this approach is to determine the optimal separating value between edge and non-edge. In other words, this is the threshold problem and the second order partial derivatives can overcome this. Instead of imposing a threshold value in the first order partial derivatives of the image, it is better to find the points where the images has the maximum rate of change. These points are the zeros of second order partial derivatives. The second order partial derivatives can be approximated using the kernels presented in the figure 2.16

The Laplacian operator is defined as

$$\begin{bmatrix} 0 & 0 & 0 \\ -1 & 2 & 1 \\ 0 & 0 & 0 \end{bmatrix} \begin{bmatrix} 0 & -1 & 0 \\ 0 & 2 & 0 \\ 0 & 1 & 0 \end{bmatrix}$$

Figure 2.16: Kernels used to approximate the second order derivatives of a image in horizontal and vertical direction.

$$\nabla^2 f = \frac{\partial^2 f}{\partial x^2} + \frac{\partial^2 f}{\partial y^2}, \quad (2.12)$$

being f a two dimensional function. It is easily deduced that the Laplacian can be approximated using the kernel given in figure 2.17:

$$\begin{bmatrix} 0 & -1 & 0 \\ -1 & 4 & 1 \\ 0 & 1 & 0 \end{bmatrix}$$

Figure 2.17: Kernels used to approximate the Laplacian.

The main drawback of this method is its high sensibility to noise. This is usually solved using a Gaussian filter to smooth the image before applying the Laplacian operator. Due the commutative property of convolution it is equivalent to carry the convolution between the Gaussian function G and the Laplacian kernel first and then do the convolution with the image. The convolution of G with the Laplacian kernel is usually denoted by the Laplacian of Gaussian (LoG) and is an approximation to the continuous function $\nabla^2 G(x, y; \sigma)$, where $G(x, y; \sigma)$ is the Gaussian function defined in 2.4. Generally LoG uses a Gaussian function with $u_x = u_y = 0$ and $\sigma_x = \sigma_y = \sigma$. So LoG is defined by

$$\begin{aligned} LoG(x, y; \sigma) = \nabla^2 G(x, y; \sigma) &= \frac{\partial^2 G(x, y; \sigma)}{\partial x^2} + \frac{\partial^2 G(x, y; \sigma)}{\partial y^2} \\ &= (\frac{x^2}{\sigma^4} - \frac{1}{\sigma^2}).\frac{e^{-(\frac{x^2+y^2}{2\sigma^2})}}{2\pi\sigma^2} + (\frac{y^2}{\sigma^4} - \frac{1}{\sigma^2}).\frac{e^{-(\frac{x^2+y^2}{2\sigma^2})}}{2\pi\sigma^2} \\ &= (\frac{x^2+y^2}{\sigma^4} - \frac{2}{\sigma^2}).\frac{e^{-(\frac{x^2+y^2}{2\sigma^2})}}{2\pi\sigma^2} \ . \end{aligned} \quad (2.13)$$

2.2.2.4 Blob Detection

In 1994 Lindberg [Lin94] introduced the scale-space theory where an image I has several scale representations denoted by

$$L(x, y, s) = G(x, y; \sqrt{s}) * I(x, y), \quad (2.14)$$

being $s = \sigma^2$ the scale. This set of representations is useful to detect features or objects in a image. One type of objects that can be detected are the blobs (objects almost circular with low contrast). As Lindberg showed [Lin93] the LoG filter is not only useful to detect edges but also blobs.
In figure 2.18 it is given the 3D representation of the LoG function, enabling a better understanding of why the LoG shoot attains an extremum response when aligned with the center of blob in an image. Bright blobs will originate minima, whereas dark blobs originate maxima. The value of

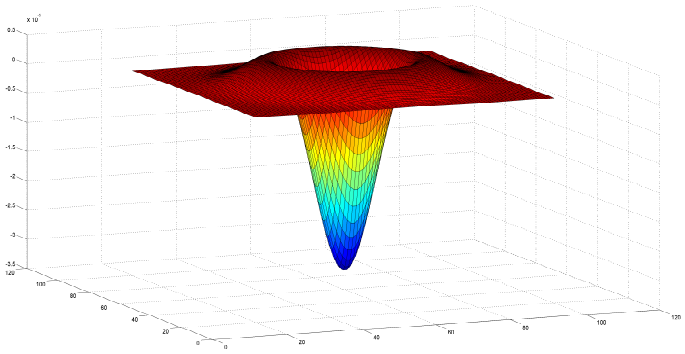

Figure 2.18

$\int_{-\infty}^{\infty} \nabla^2 G(x, y; s)$ is 0, whereat the response of LoG will be more closer to 0 as the homogeneity of a region increases. The response of LoG depends mainly on the difference between the pixel intensity values covered by the negative part and the positive part of LoG filter. The response will be stronger as this difference increases. As blobs are characterized by a strong difference between them and the background, they correspond to strong LoG responses. The negative part of LoG lies in a circle located in the center of the LoG filter, while the positive part is beyond that circle. Assuming that blobs are dark and the background is white, the LoG filter that has the strongest response to a blob with radius r is the LoG which negative part has also a radius r. In order to determine the value of s that defines the best LoG that detects blobs of radius r, the following equation needs to be solved:

$$\begin{aligned}
\nabla^2 G(x, y; \sqrt{s}) = 0 \iff \\
(\frac{x^2+y^2}{s^2} - \frac{2}{s}).\frac{e^{-(\frac{x^2+y^2}{2s})}}{2\pi s} = 0 \iff \\
(\frac{x^2+y^2}{s^2} - \frac{2}{s}) = 0 \vee \frac{e^{-(\frac{x^2+y^2}{2s})}}{2\pi s} = 0 \iff \\
\frac{x^2+y^2}{s^2} = \frac{2}{s} \vee (x, y) \in \emptyset \iff \\
x^2 + y^2 = 2\ s \iff \\
r^2 = 2\ s \iff \\
r = \sqrt{2s}\ .
\end{aligned} \tag{2.15}$$

This relation is useful to determine the value of s to locate blobs with an approximate radius r. Besides, it can be used to determine the radii of the objects detected when the s of the LoG is known.

Using all this information Lindberg established that the blobs in an image could be detected using the extreme values of the three dimensional space volume $\nabla^2 L(x, y; s)$.

$$\nabla^2 L(x, y, s) = \nabla^2 G(x, y; \sqrt{s}) * I(x, y) = LoG(x, y; \sqrt{s}) * I(x, y). \tag{2.16}$$

In each layer of $\nabla^2 L$ controlled by s it is expected that blobs with radius $\sqrt{2s}$ have a higher response than in others layers. However, the response of the LoG filter decreases as s increases what leads to problems when comparing the values between different scales. To solve this a normalized scale

space is used.

$$\nabla^2_{norm} L(x, y; s) = s\nabla^2 L(x, y; s). \quad (2.17)$$

2.2.2.5 Difference of Gaussians (DoG)

The DoG is a filter that tends to attenuate objects which size does not belong to a selected range of sizes [MH80]. In the frequency space it is a band pass filter and is defined by:

$$DoG(x, y; \sigma_2; \sigma_1) = G(x, y, \sigma_2) - G(x, y, \sigma_1). \quad (2.18)$$

Using this definition it can be shown that DoG and LoG are related. Assuming that $\sigma_1^2 = s$ and $\sigma_2^2 - \sigma_1^2 = \Delta s$ the derivative of a Gaussian function $G(x, y, s)$ with respect to s can be defined as

$$\begin{aligned} \frac{\partial G(x, y, s)}{\partial s} &\approx \frac{G(x, y, s + \Delta s) - G(x, y, s)}{\Delta s} \\ \frac{1}{2}.(\frac{x^2 + y^2}{s^2} - \frac{2}{s}).\frac{e^{-(\frac{x^2+y^2}{2.s})}}{2\pi.s} &\approx \frac{DoG(x, y; s)}{\Delta s} \\ \frac{\nabla^2 G(x, y, s)}{2}.\Delta s &\approx DoG(x, y; s)\ , \end{aligned} \quad (2.19)$$

As σ_2 can be expressed as a multiple of $\sigma_1, \Delta s = (k.\sigma_1)^2 - \sigma_1^2$

$$\begin{aligned} \frac{\nabla^2 L(x, y, s)}{2}.(k^2 - 1).\sigma_1^2 &\approx DoG(x, y; s) * I(x, y) \\ \nabla^2_{norm} L(x, y; s).\frac{k^2 - 1}{2} &\approx DoG(x, y; s) * I(x, y)\ . \end{aligned}$$

2.2.2.6 Hough Transform

In some kind of problems the shape of objects that needs to be detected is *a priori* known. In these cases, using methods that search certain type of shapes can be more useful than more general techniques. The Hough transform was originally proposed by Paul Hough[Hou59] to detect lines in images and extended to other shapes by R. Duda and P. Hart [DH72]. The basis of this method is the assumption that the points that define a shape on an image are edge points and they can be used to parametrize the shape. Each one of the edge points votes on the several parameters that define a shape that contains that point. After all the points vote, the most likely shapes in the image are expected to be the most voted. Although this technique may be very accurate in finding particular shapes it has the disadvantage of demanding a lot of processing, i.e., a very high computational burden. As the degrees of freedom of the shape increase, the computational burden attains unaffordable times of processing. This way, the Hough transform is generally used to detect only simple shapes or complex shapes with a lot of constraints.

2.2.3 Segmentation

2.2.3.1 Region Growing

This segmentation technique was originally proposed by Adams and Bischof[AB94] and aims to gather pixels that share certain types of features and group them into regions. It is assumed that the regions are connected and disjoint. In order to start the construction of the regions, the

algorithms needs initial *seeds*. Each *seed* is a region that will expand, gathering to it pixels that are connected to the region and share the same feature. The regions can merge if they have similar features and should stop expanding when no more pixels could be gathered. This algorithm is very useful when there are small interesting regions in the image that are confused with noise by the threshold algorithms. Adams and Bischof proposed the mean of region to be the feature that controls the join of the pixels to each region. With this algorithm proposed they were able to segment correctly X-ray images of the human chest.

2.2.3.2 Watershed

The idea that a image can be viewed as a topographic surface gave birth to this algorithm [BL79]. In a gray-scale image each intensity represents the height of the surface on the position (x, y). The aim of watershed algorithm is to find the boundaries of each region on the image. In order to achieve it the regional minimums of the image are used as seeds, expanded as if the water started to flood the topographic region entering in minimums points. The boundaries will be defined as the dams that need to be constructed to avoid the merging of two expanding regions. This technique tends to oversegment the image, creating more regions than the existing. This is due to the fact that some local minimums may be part of the noise in the image and should be ignored by the watershed algorithm. To overcome this problem marked seeds are used, instead of the regional minimums of the image [MB90]. Figure 2.19b illustrates the result that can be obtained from the original image (figure 2.19a) if the seeds are correctly marked.

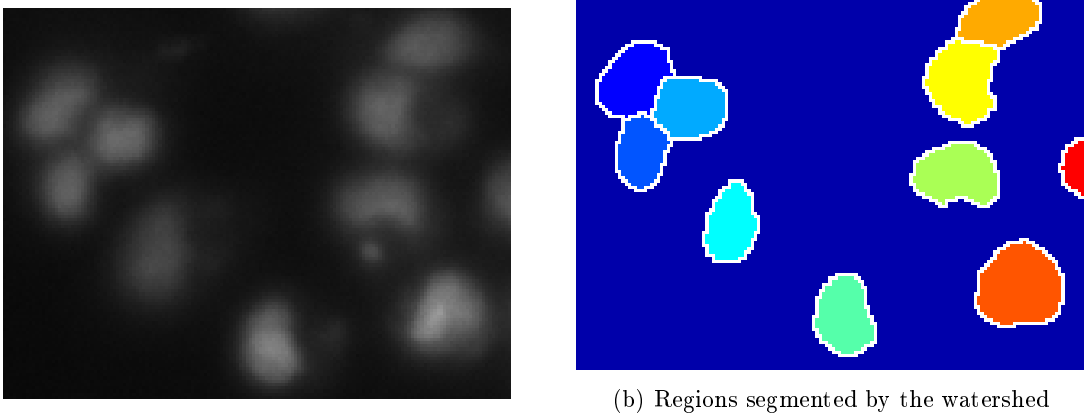

(a) Image cointaining only macrophages .

(b) Regions segmented by the watershed algorithm using initial seeds.

Figure 2.19: Result of watershed algorithm using initial seeds.

2.2.3.3 K-means

The K-means algorithm was originally proposed by Stuart Lloyd[Llo82] to partition n observations into k sets, designed as clusters. The observations should be partitioned in a way such that

$$\sum_{i=1}^{k} \sum_{\mathbf{x}_j \in S_i} \|\mathbf{x}_j - \boldsymbol{\mu}_i\|^2, \quad (2.20)$$

is minimized, where x_j is an observation. S_i and $\boldsymbol{\mu}_i$ are the set of observations and the mean of the i^{th} cluster, respectively. Although this algorithm is commonly used to perform the clustering of data, it can be also useful in the segmentation as shown by Proença *et* al.[PA06]. Features (e.g.

pixel intensity, texture, color intensity) can be extracted from small regions of image or even pixels, yielding an observation for each considered region. Applying the k-means algorithm to these data, the image is divided into k clusters representing the final segmentation.

2.2.4 Encoding and Normalization

After perform the detection of the ROI and use it as the source for the segmentation algorithms it is expected that regions of pixels were obtained. Usually the plane comprises the extraction of relevant features from these regions. These features are used in the classification, as for example to determine how many cells exist in a region.

2.2.4.1 Region Descriptors

The region descriptors are used to measure properties of a region. These descriptors aim mainly to analyse the texture of the region. The main region descriptors are listed here, using $R(x, y)$ as the set of pixels (x, y) that belong to the region :

Area

The area can be calculated in the discrete domain as the number of pixels that belong to R.

Perimeter

In order to calculate the perimeter in the discrete domain the n pixels from the boundary are used.
$P(R(x,y)) = \sum_{i=1}^{n} \sqrt{(x_{i+1} - x_i)^2 + (y_{i+1} - y_i)^2}$

Compactness

This descriptor measures how compact is a region using the circle as a comparator. The compactness is defined as $C(R(x,y)) = \frac{4\pi.A(R(x,y))}{P(x,y)}$. It is easily deducted that $C \in [0,1]$ and every circle has $C = 1$. So the more $C(R(x,y))$ is closer to 1 the more the region is compact.

Orientation

It correspond to the angle between the x-axis and the longest chord of the region.

Euler Number

Is defined as the difference between the number of connected objects and the number of holes that exist in the regions.

Minimum Bounding Box

This descriptor measures the size of the minimal box that encloses the region.

2.2.4.2 Shape Descriptors

The shape descriptors are focused in the boundary of the region and the characteristics of the shape of the region.

Fourier Descriptors The Fourier descriptors [Gra72] are a popular method to encode the shape of a region due to their invariance to translation, rotation and scaling. In order to obtain the Fourier descriptors of a region it is necessary to describe the shape by a one dimensional function, usually called shape signature. Several types of shape signatures were proposed: curvature function, tangent angle function and complex coordinates are examples of the most common used. For every kind of shape signature, a periodic discrete function $f[t]$ is obtained. Using the Fourier transform

the function f can be approximated using a sum of functions of family e^{ix} weighted by a set of complex coefficients c_k.

$$f[t] = c_0.e^{i.0.t} + c_1.e^{i.\frac{2\pi}{N}.t} + c_2.e^{i.\frac{4\pi}{N}.t} + ... = \sum_{k=0}^{N-1} c_k.e^{i.\frac{2\pi.k}{N}.t}. \quad (2.21)$$

These weights are obtained with

$$c_k = \sum_{t=0}^{N-1} f[t].e^{-i.\frac{2\pi.t}{N}.k}, \quad (2.22)$$

and this set of weights are called the Fourier descriptors.

Using the complex coordinates as a shape signature the function f is defined by $f[t] = x_t + y_t.i$, where x_t and y_t are the coordinates of points that define the shape sampled clockwise. With this type of signature f will depend on the starting point chosen. Figure 2.20 illustrates the contour of the nucleus of a macrophage and the starting point chosen is $f[0]$. Besides that, the values of c_k will not be invariant to the translation, scaling and rotation. In order to achieve this invariance it is necessary to do a normalization step after compute the Fourier descriptors. If $f1$ and $f2$ are shape signatures, and $f2$ is the translation of $f1$ by a vector $\vec{t}$, their Fourier descriptors only differ in the first descriptor and the relation is given by $c1_0 = c2_0 + N.\vec{t}$. So, in order to normalize the fourier descriptors to translation, the value of c_0 can be always set 0. This will cause the shape to have his centroid in position $(0, 0i)$. To normalize with respect to scale it is important to know that if $f1$ and $f2$ are related as $f1 = s.f2$ then $c1_k = s.c2_k$. Hence scale invariance can be obtained with $\frac{c_k}{|c_1|}$. The invariance to rotation can be achieved by determining the angle α of the largest radius with the x-axis. Then $e^{i.\alpha}.c_k$ will be invariant to rotation. The invariance to the starting point can be obtained by choosing the point that is more distant from the centroid.

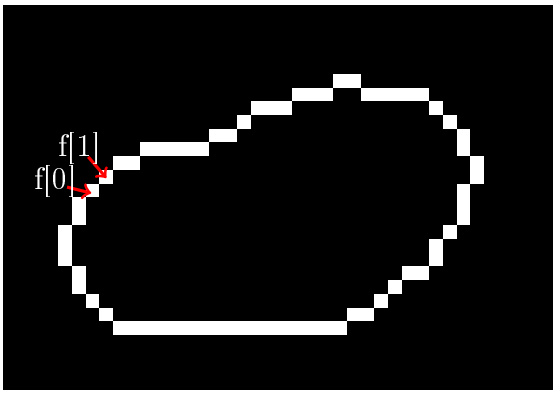

Figure 2.20: Contour of a macrophage nucleus and the first two sampled points used to define the shape signature ($f[0]$ and $f[1]$).

The normalized Fourier descriptors are useful to identify shapes and match them. Their invariance ensures that shapes that differ by affine transformations will have the same descriptors. Besides, similar shapes will have similar descriptors what can be useful to match objects with a desired shape.

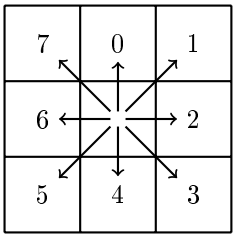

(a) The codes used in 8-connected

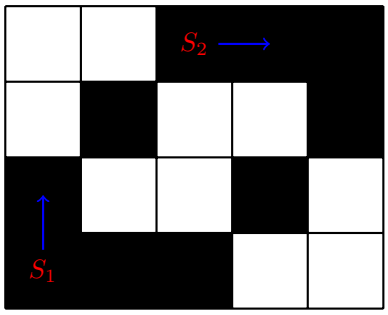

(b) Boundary of a region and the corresponding chain codes with different starting ponints $S1$ and $S2$.

Figure 2.21: Example of chain codes using 8 connected neighbours.

Chain Codes The Chain Codes were introduced by Freeman [Fre61] in order to describe a region by a code. This codification is not only useful to allow compression of the data but also synthesizes the shape of a region. This type of encoding uses the boundary of a region to describe the direction from each point of the boundary to its neighbour. In the Freeman proposal could be used 4 or 8 connected neighbours and the starting point could be any point of due to the fact that normalized chain codes are invariant to the starting point. In figure 2.21a it is given the mapping between the directions and the code used in 8 connected neighbours and figure 2.21b illustrates the boundary of a region and chain codes obtained when the starting point chosen is $S1$ or $S2$.
The codes originated from different start points are different, but if normalized their invariance to the starting point can be guaranteed. This step consists in shifting the code until the digits of the code form the lowest integer possible. In the case presented in figure 2.21b the code originated by using $S1$ as a starting point is already the normalized chain code of the boundary. Besides this, the invariance to rotation can be also achieved by mapping the highest digit in the code to 0 and do an equivalent mapping for the remaining digits. These properties make the chain codes a useful tool to define and compare objects.

Shape Context In 2000, Belongie and Malik [BMP02] proposed the shape context descriptor to recognize objects. Although this descriptor is a small part of their work, it can be used in other approaches because it is able to synthesize quite well the main shape of an object. The shape context descriptor uses n points from the boundary sampled with a constant frequency. For each point p_i in the boundary it must be computed the $n-1$ vectors formed by p_i and the remaining points of the boundary. The directions and the norms of the vectors are used to construct the log polar histogram that represents the shape context of the point p_i. Figure 2.22 illustrates the boundary points of a square and $n-1$ vectors obtained from the point p_i. The figure depicts well the several bins that were created by the log polar referential. The log polar is constructed by accumulating the amount of points that fall in each bin.
The set of log polar histograms represents the encoded form of a shape. In order to obtain the similarity of two shapes, Belongie and Malik used an approach based on bipartite graph matching algorithms. Each point of the first shape is matched with other point of the second shape so that the total cost of the match is minimized. The cost of assign a point p_i on the first shape to a point q_i on the second shape is given by the Chi-square distance between the log polar histograms of p_i and q_j.

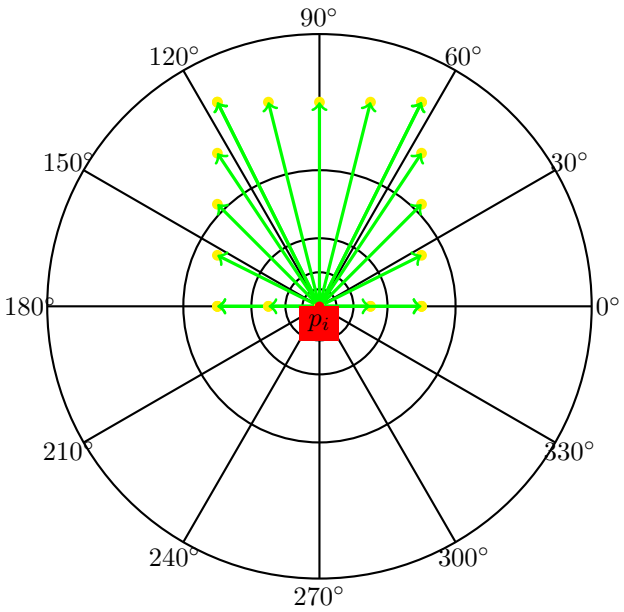

Figure 2.22: Example of the log polar referential used to construct the log polar histogram.

$$C(p_i, q_j) = \frac{1}{2}\sum_{k=1}^{K}\frac{[h_i(k) - q_j(k)]^2}{h_i(k) + q_j(k)}, \quad (2.23)$$

where K is the number of bins of p_i and q_j. The difference between the shape p and q is given by

$$D(p, q) = min(\sum_{i=0}^{N} C(p_i, q_j)), \quad (2.24)$$

where N is the number of points in each shape.
This method is very useful to identify what is the most likely class of an object, given a set of known classes due to the fact that two objects whose shapes share the same main characteristics will have a small value of D.

2.2.5 Matching and Classification

After an object O is encoded and normalized the usual approach is to compare the encoded values that represent O with a database of known objects. This comparison aims to find the most similar object in the database and use its class to classify O. In this phase it is very usual to use a machine learning approach. In the case of supervised problems algorithms as Support Vector Machines (SVM) [CV95], artificial neural networks [RHW86] are among the most popular. The supervised algorithms learn how to classify new instances using a set of previous classified instances, called the training data. However, the efficiency of these algorithms is always dependent on the features retrieved from the objects. These features must be discriminant, in other words, they should allow to distinguish a object between the classes. If the training data is not labelled, the problem is unsupervised and in this case the algorithms aim to gather the data in clusters based on the characteristics of each instance. K-means [Mac67], Self-organizing maps[Koh88] and the Mixture Models using expectation maximization [DLR77] are examples of unsupervised algorithms.

2.3 Related Work

In the literature, cell detection/counting has been approached in several works [TUG02, HKB+11, SM06, MFRS08]. In the majority of the cases, the authors devised new methods to segment and split overlapped cells ([KGBB11]), since it represents the main factor for performance degrading. Cell segmentation is also used when the aim is delineate cell regions. The seeded watershed transform is a common choice to this end ([LWBZ04]). [HPH+11] compared the maximum-intensity linking (MIL) method with the watershed transform and reported better results with MIL on the segmentation of HeLa cells. Watershed transform and MIL exploit the fact that the intensity of fluorescence-stained cells usually decreases from the core to the boundary. In *Leishmania* infections this is not always true due to cells with multiple nuclei, what prevents the use of such techniques in our type of images.

Contour analysis can provide a correct handling of these cases and has also been used in cell counting approaches. Fok *et* al. [FCC96] proposed a method to count the number of axons in nerve cells based on active contours. Due to the typical shape of the axons, the Hough transform for elliptical shapes is initially used. The result of the Hough transform is then used as the initial guess for the frontier of each axon. Active contours are fed with this initial guess and used to delimit the outer and inner boundaries of the membrane that surrounds each axon, the myelin. The number of axons is not the only output of this system but also the characteristics of the myelin. This justifies the importance of active contours in this task.

Kharma *et* al. [KMY+07] performed an automatic segmentation of cells using microscope images . Two main phases are described. The first aims to extract the cells from the background combining an adaptive threshold with morphological operators. The binary image that results from this process is expected to have the cells separated from the background. However, this phase detects clusters of cells, in case of cell overlapping. The second phase is oriented to overcome this problem. Supposing that the general shape of cells is an ellipsis, a genetic algorithm is used to search the parameters that define the set of ellipsis that best fit a clustered region of cells. Each ellipsis found defines a cell and its segmentation.

Faustino *et* al. [FGRdL09] developed a method to detect and count stem cells in fluorescence images. An adaptive threshold separates the cells from the background and the histogram of the image is employed to create several classes in the regions detected. The histogram is partitioned in equal size intervals creating different classes in each connected region. The set of regions and its classes are mapped to nodes of a graph G, mined with predefined rules to perform the separation between the overlapping cells in each region.

The approach of Xiangzhi *et* al. [BSZ09] is based on the notion of concavity and assumes an elliptic shape for the cells. The contour of each cell is approximated by a polygon, so that concave points can be detected and small-scale fluctuations are avoided. The set of p concave points divide the contour into p segments. For each segment, the best fitting ellipse is found using the algebraic distance as a fitting metric. The resulting ellipses are subjected to a selection process, in order to remove the ellipses with distance higher than a threshold. Next, the selected ellipses pass through a combination step, in order to determine which segments regard the same cell. Finally, the remaining ellipses delimit the contours of each cell.

Although these methods had achieved good performances, they were not devised to deal with specificities of *Leishmania* infections.

To the best of our knowledge, the automatic annotation of *Leishmania* infections in fluorescence microscopy was only addressed in two different approaches: Nogueira's approach and Leal *et* al.'s approach.

2.3.1 Nogueira Method

Pedro Nogueira proposed a method to automatically determine *Leishmania* infection levels in fluorescence images [Nog11]. Each channel is used independently to detect macrophages and parasites. Otsu's method is used to separate the objects in each channel from the background. The majority of the image has a bimodal distribution enabling a good separation between the objects and the background. However there are some cases in which the distribution is multimodal due to noise. A routine to analyze the histogram monotony was proposed, determining the number of modes in the histogram. The extended Otsu's method[LCC01] is used to binarize images with distributions with more than two modes. The binarized channel that results from this process is used to extract features from each one of the connected components, designed as regions. Each region is a cluster of k nucleus or parasites that occur due to the overlapping of objects. Features as the area and the center of mass are extracted from the region, assuming that they can be discriminant in what concerns the number of objects present. A machine learning approach is used to predict the value of k for each region given a set of features. A SVM was trained for this task along with a rule-based statistical classifier. A voting system is then used to conciliate the predictions of the classifiers. At last, each region is de-clustered with Gaussian Mixture Models (GMM) using k mixtures. In figure 2.23 the de-clustering results obtained with the GMM is illustrated. In on of the cases, the method was able to determine the existence of four nuclei, whereas in the other the de-clustering was not successful.

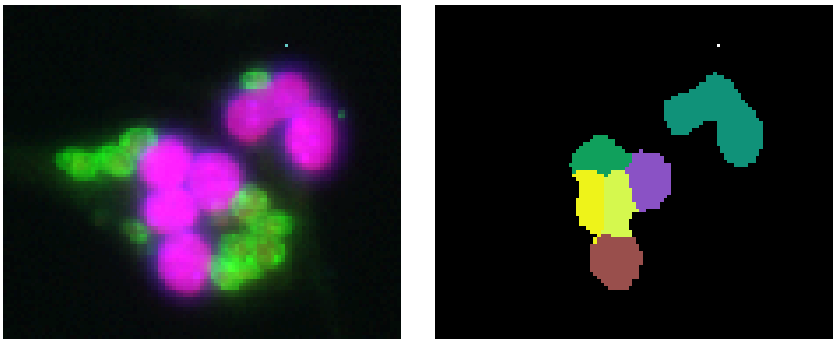

(a) Part of an original image. (b) Results of nuclei de-clustering.

Figure 2.23: Results of the de-clustering process used for nuclei detection.

Once the nuclei and parasites detection is performed, the authors associated each parasite with the nearest nuclei, unlike the process carried out by the biologist, that use the cytoplasm.

2.3.2 Leal *et* al. Method

In [LFM+12] Leal *et* al. proposed an method to annotate automatically microscope images with *Leishmania* infections. This method is based in the DoG filter and in its capacity to select objects of certain scales. The main idea behind this method is that the nucleus have almost all the same size. Using the DoG as an approximation of LoG [Lin94] it is possible to filter the image and obtain an image F_σ where blobs with radius $\sqrt{2}\sigma$ (equation 2.15) are enhanced. In order to estimate the correct value of σ, designated hereinafter as $\sigma_{correct}$, an iterative approach was built. In each iteration, the image is filtered with a DoG filter using standard deviation of σ_{old}. The filtered image is binarized using Otsu's method and the average size of the detected nuclei, designated as $\boldsymbol{\mu}_N$, is determined. The authors used the relation $\bar{\sigma_d} = \frac{\boldsymbol{\mu}_N}{4}$ to infer the average σ associated with the detected nuclei. The new value for σ is updated:

$$\sigma_{new} = 0.7\sigma_{old} + 0.3\bar{\sigma_d}, \quad (2.25)$$

based on the idea that σ_{new} must increase if $\bar{\sigma_d} > \sigma_{old}$ and vice versa. The process is repeated until $|\frac{\sigma_{new}-\sigma_{old}}{\sigma_{old}}|$ converges to a stable solution. It is expected that the value of σ converges to $\sigma_{correct}$ independently of the initial guess, as evidenced in the figure 2.24.

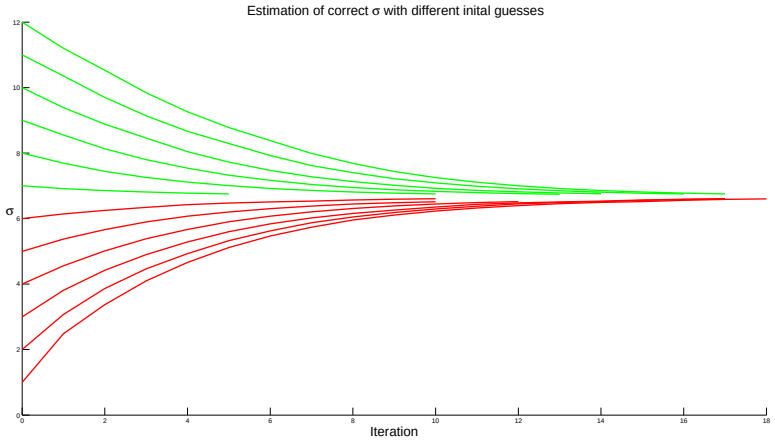

Figure 2.24: Results obtained by the method proposed by Leal *et* al. to infer the value of $\sigma_{correct}$ using different initial values for σ. Red and green curves represent the evolution of σ when the initial value was lower than and higher than $\sigma_{correct}$, respectively.

The visual illustration of this idea is presented in figure 2.25, where an initial guess of $\sigma = 15$ (higher than the correct value) was used. The top figures represent the intensity map of $F_{\sigma_{old}}$, whereas the bottom figures denote the binarized version of the top figures.

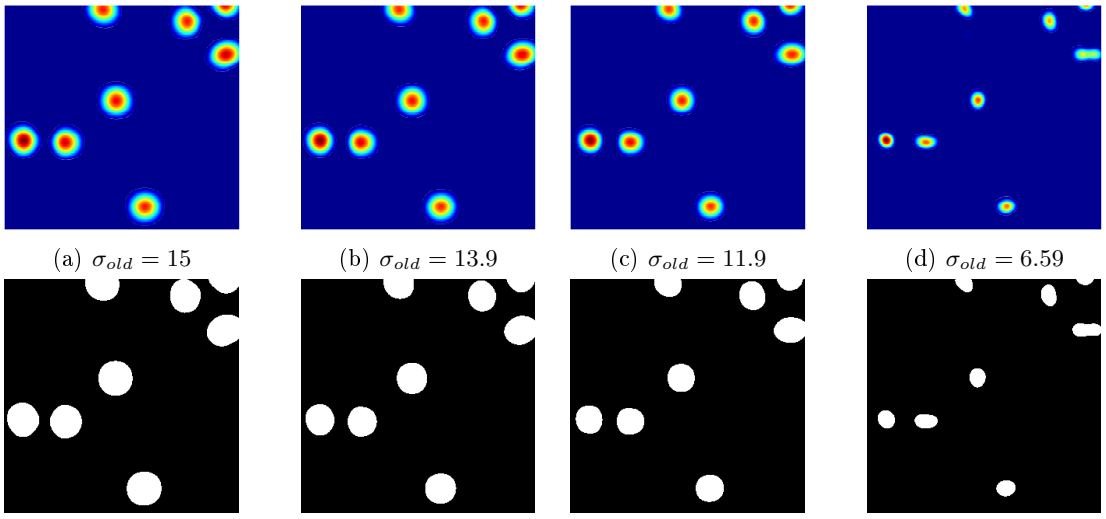

(a) $\sigma_{old} = 15$ (b) $\sigma_{old} = 13.9$ (c) $\sigma_{old} = 11.9$ (d) $\sigma_{old} = 6.59$

(e) $\sigma_{new} = 13.9$ (f) $\sigma_{new} = 11.9$ (g) $\sigma_{new} = 11.1$ (h) $\sigma_{new} = 6.57$

Figure 2.25: Illustration of F_σ (top) and the binary versions of F_σ (bottom) for some iterations of the iterative process devised to infer the correct value of σ.

The top figures were obtained using the DoG filter with a standard deviation of σ_{old}, however as this value is higher than the correct, the value of $\bar{\sigma_d}$, determined by the binary images, is lower than σ_{old}, yielding a lower σ_{new}. When the difference is residual and stable, (figures 2.25d and

2.25h), the binary image corresponds to the final segmentation of nuclei. The detection of parasites body is done in a similar way to the macrophages nucleus. After this, it is necessary to perform the associations between macrophages and parasites. In this method this is done using the cytoplasm that corresponds to each one of the nucleus. This is the same process that parasitologists use to associate macrophages and parasites, explained in subsection 2.1.4. The cytoplasm is segmented with an approach that combines the seeded watershed algorithm and Otsu's method. The centroid of each detected nucleus is used as seed of the watershed algorithm. The result of watershed is then pruned with the binary image, that is obtained by applying the Otsu's method to the preprocessed macrophages channel. The set of pixels that belong to the background in the binary image are also labelled as background in the result of watershed. With this, the cytoplasmic frontiers between the background and the macrophages and also between macrophages are defined. The association can now be performed and the infections rates calculated.

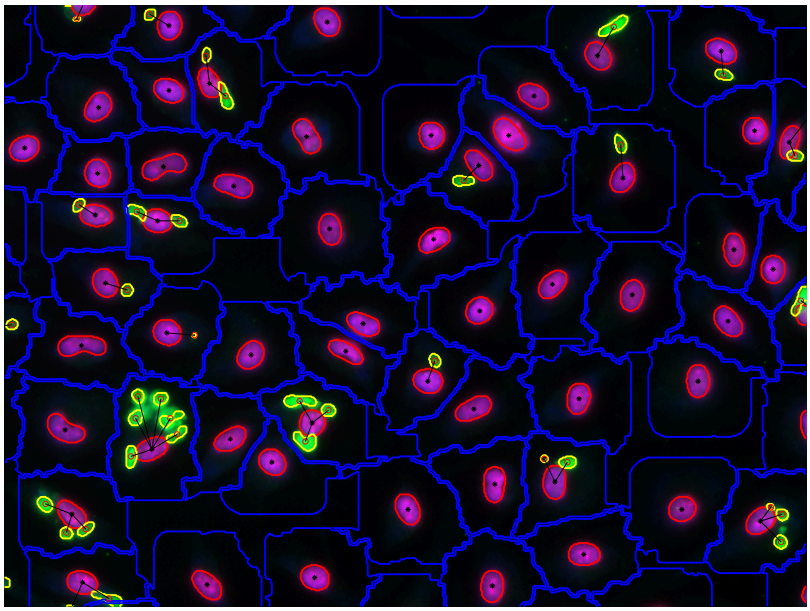

Figure 2.26: Results obtained with Leal *et* al.'s approach. The boundaries of the sevral cellular data present in the image are depcited with different colors.

Figure 2.26 depicts the final results of this process. In red and yellow colors are given the boundaries of the detected nuclei and parasites, respectively. The cytoplasm boundaries, obtained with the watershed algorithm, appear as blue. The cytoplasmic regions were used to determine the infecting parasites of a macrophage, and are represented as black lines between the centroids of nuclei and parasites.

Chapter 3

Proposed Method

In this chapter we describe the method proposed to perform the detection and separation of cells in images with *Leishmania* infections, together with the rationale for each of the choices made. Our approach can be divided in seven main phases: Pre-processing, Blob Detection, Cytoplasm Segmentation, Contour Smoothing, Matching Process, Refinement Process and Association process. Figure 3.1 illustrates the workflow of macrophage processing (Figure 3.1a) and parasites processing (Figure 3.1b). In the later case, an additional phase was proposed. Each phase contains a different challenge and we have devoted one section per phase so that it could be explained how we addresses it.

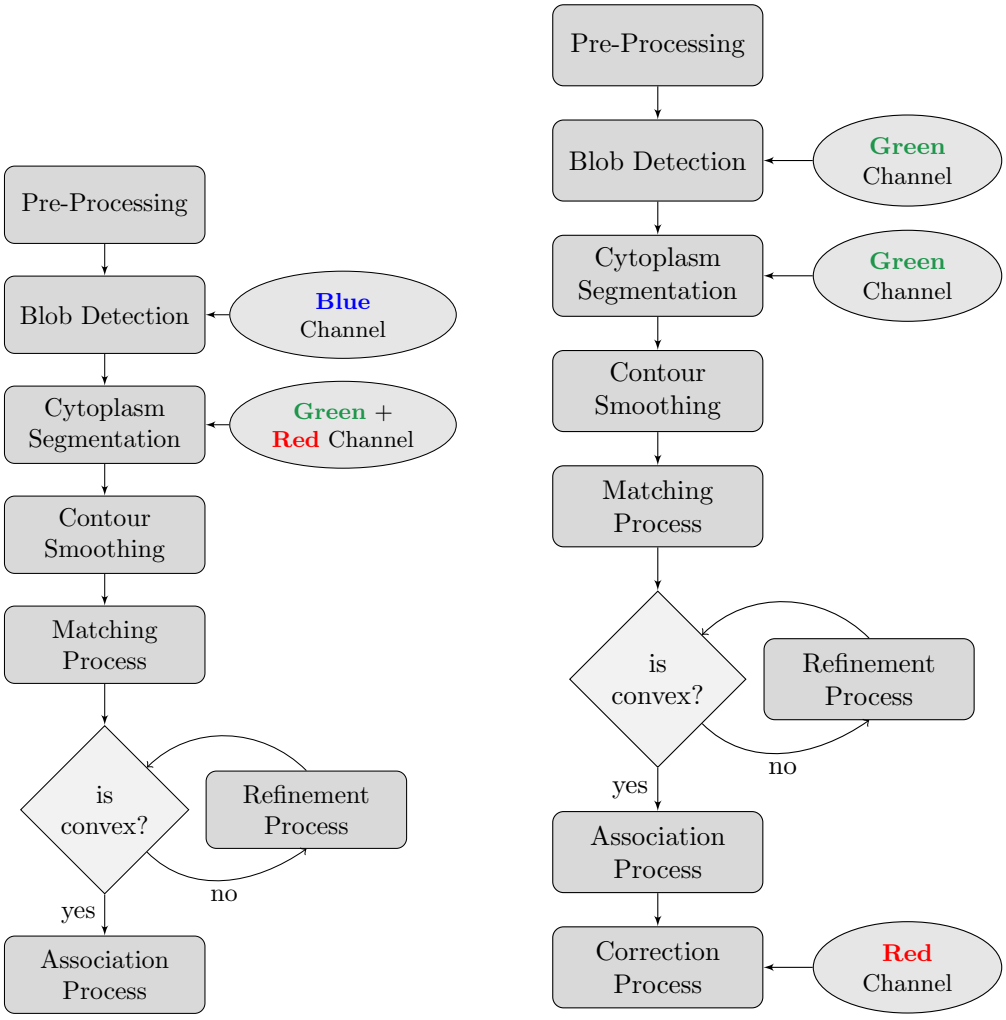

(a) Macrophage Process

(b) Parasite Process

Figure 3.1: Diagram of the workflow in a) macrophage and b) parasite procesing.

3.1 Pre-processing

In order to enhance and highlight discriminant patterns, in what regards the aims of the work, pattern analysis should be preceded by the pre-processing of data. As mentioned before, the images acquired by Carl Zeiss microscopes [Zei13] are recorded in a proprietary format. ZVI data are not normalized and have low contrast. Aiming at solving these issues, we used a contrast stretching step in each channel. With this, cellular organisms were enhanced, what may improve the detection performance.

3.2 Blob Detection

The ultimate goal of this work was to locate correctly the positions of the macrophages and parasites in an image, and perform their association. In what concerns the tracking of macrophages and parasites, we found the blob detection, proposed by Lindberg [Lin94], useful to provide the macrophages and parasites locations. The general shape of macrophages and parasites is almost circular, and their contrast with the background allowed us to consider them as blobs. As explained in the subsection 2.2.2.4, the locations and scales of the blobs in an image I were approximated by inspecting the local extrema of the three dimensional space volume $\nabla^2 L(x, y; s)_{norm}$. Supposing that the radius of the desired blobs is in the interval $[r_{min}, r_{max}]$ we defined $SS(x, y; r)$ as

$$SS(x, y; r) = \nabla^2 L(x, y; \frac{r^2}{2})_{norm},\ r \in \{r_{min}, r_{min} + 1, \ldots, r_{max}\}, \quad (3.1)$$

Macrophages nucleus and parasites cytoplasm are both brighter than the background, so their locations and corresponding scale were given by the set of points $p = (x, y; r)$, such that $SS(p)$ is a local minimum (refer to 2.2.2.4). The search of local extrema was done not only along the space dimensions but also over scale, justifying the use of the scale normalized LoG filter (LoG_{norm}). Instead of using a neighbourhood of $[x, y, r] = [3, 3, 3]$ to determine the local minima, we used a Heaviside function $H(x, y, r)$ to determine the local minima:

$$H(x, y, r) = \begin{cases} 1 & \text{if } SS(x, y; r) > SS(a, b, c),\ \forall\{a, b, c\} \in \zeta(a, b, c) \\ 0 & \text{otherwise} \end{cases},$$

where $\zeta(a, b, c)$ gives the discrete neighbourhood, i.e., $a \in \{x-1, \ldots, x+1\} \setminus \{x\}$, $b \in \{y-1; \ldots, y+1\} \setminus \{y\}$, and $c \in \{r_{min}, \ldots, r_{max}\} \setminus \{r\}$, and "\" denotes exception. Some local minima may not correspond to a real blob, but to noise in the image. They can be distinguished by the magnitude of the filter response. In our approach, the suppression of false maxima was performed using the image background and a parameter ε (refer to section 4.2). The segmentation of image background was achieved using an adaptive threshold algorithm [Nob79], yielding a function $B : \Omega \to \{0, 1\}$, where 0 denotes the background. The maxima that do not lie in the background were normalized using the min-max rule. The final set of detections are given by

$$M = \begin{array}{l} \{p = (x, y; r) \in \mathbb{R}^3 : H(x, y, r) = 1, \\ B(SS(p)) \neq 0 \wedge SS^*(p) < -\varepsilon\} \end{array}, \quad (3.2)$$

where SS^* denotes the normalized value according to the min-max rule.
We denote the set of blob locations in M as $\{(x_1, y_1), ..., (x_n, y_n)\}$. Blob detection was performed in the blue and green channel to determine the macrophages nuclei and parasites cytoplasm,

respectively, as in these channels cellular elements can be easily distinguished, as explained in 2.1.3.

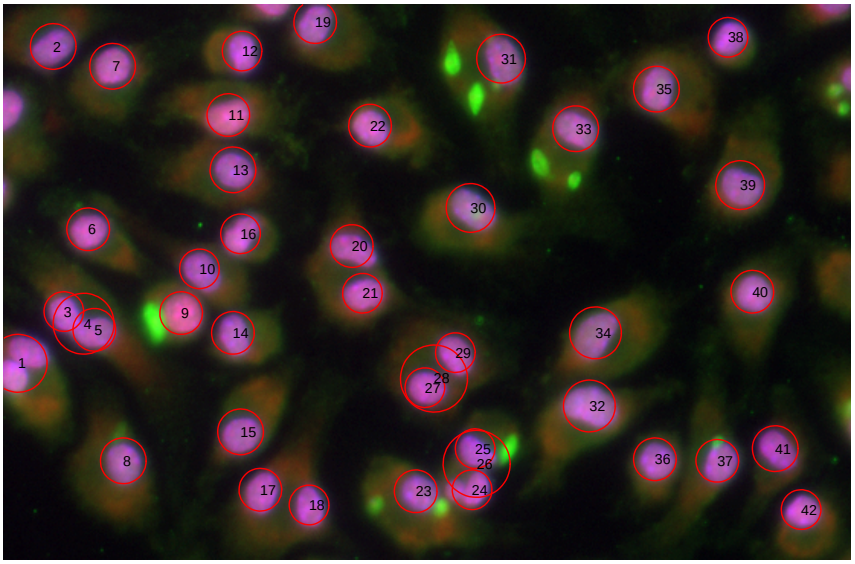

Figure 3.2: Results obtained for macrophage nucleus detection.

Figure 3.2 illustrates the results obtained using our blob detection phase. Each red circle denotes a blob contained in M. This approach yields correct detections in a majority of the macrophages and parasites, however it fails when the nuclei are too close, as it be observed in the 24^{th}, 25^{th} and 26^{th} blobs.

3.3 Cytoplasm Segmentation

As the detections performed by the previous phase may overestimate the real number of cellular data, we tried to perform the cytoplasm segmentation in order to validate or reject the detections obtained by the blob detection. Multiple detections at the same cell could be easily discarded if they lie on the same cytoplasm. Based on this idea, we aimed to segment the cytoplasmic area correspondent to each blob in M. Let Ω_i be a subset of Ω. For each blob in M a region of interest (ROI) was gathered from the green channel with center at (x_i, y_i). The ROI of the i^{th} element of M was denoted by R_i. In order to segment the cytoplasm in R_i, a clustering algorithm maps each pixel to one of k clusters, using a function $T : \mathbb{R} \rightarrow \mathbb{N}^+$, such that:

$$T(a) = \arg\min_i |a - c_i|, \quad (3.3)$$

where c_i are the centers given by the clustering algorithm. In our experiments, the K-means with $k = 3$ was used (refer to section 4.2 for the proper justification). The clustered ROI is given by

$$R_{ic}(x, y) = T(R_i(x, y)). \quad (3.4)$$

From R_{ic}, we obtain the set of pixels inside the cytoplasmic area by applying $T_b : \mathbb{N}^+ \rightarrow \{0, 1\}$.

$$T_b(x) = \begin{cases} 0 & \text{if } x < t \\ 1 & \text{if } x \geq t \end{cases}, \quad (3.5)$$

being t the cluster with lowest average luminance that contains cytoplasmic areas. We used $t = 2$ macrophages and $t = 3$ for parasites, since the parasites cytoplasm is usually brighter than the macrophage cytoplasm. The result of applying T_b to R_{ic} yields B_{ic}, that contains the cytoplasmic areas, and is formally defined as

$$\Omega_{ij} \in \Omega_i \text{ such that } \bigcap_j \Omega_{ij} = \varnothing \wedge (T_b \circ T \circ R_i)(\Omega_{ij}) = 1 \quad (3.6)$$

Among the regions in Ω_i, there exists one p such that $(x_i, y_i) \in \Omega_{ip}$. We used this value to remove from $B_{ic}(x, y)$ all Ω_{ij} such that $j \neq p$, keeping only the cytoplasmic areas that belong to the detected blob.

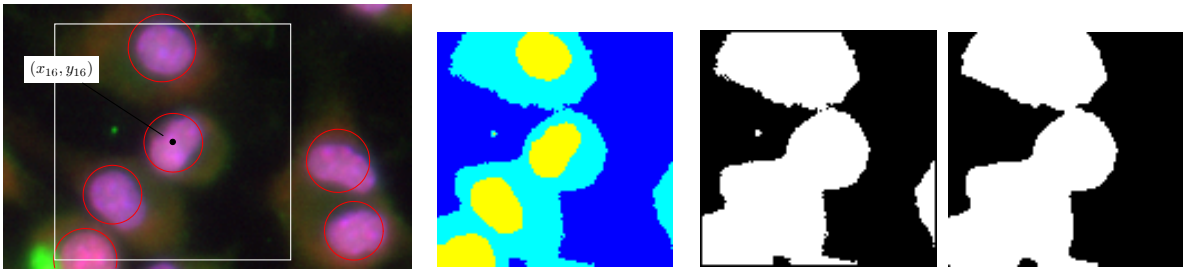

Figure 3.3: The key steps of cytoplasm segmentation phase. a) The region of interest gathered for a blob. b) The clustered ROI. c) The cytoplasmic areas obtained with the transformation T_b. d) The cytoplasmic areas associated with the 16^{th} blob.

Figure 3.3a) illustrates the ROI gathered for the 16^{th} blob (white). $R_{16\ c}$ is presented in the figure 3.3b), where each colour represents a cluster. The cytoplasmic areas were obtained with the transformation T_b, yielding B_{16c}, figure 3.3c). The only region that contains the blob center is presented in the figure 3.3d).

3.4 Contour Smoothing

After the cytoplasm segmentation phase, we obtained a set of ROIs containing, each one, a Ω_{ip}. The region Ω_{ip} contains the cytoplasmic area of the i^{th} blob. However, due to overlapping, it may also contain the cytoplasm of other cells. In order to perform the separation of overlapping cytoplasms, we developed an approach based on the concave points of the contour. The contour of Ω_{ip} is given by

$$c(t) = (x(t), y(t)), t \in \{0, 1, ..., L\}, \quad (3.7)$$

where L is the length of the contour. Considering the discrete nature of $c(t)$, it has a lots of high frequency information that cannot be misunderstood as concave points. Due to this, elliptic Fourier

descriptors [Gra72] were used to to parametrize the contour. The Fourier coefficients $a = (a_x^{(.)}, a_y^{(.)})$ and $b = (b_x^{(.)}, b_y^{(.)})$ are determined by

$$\begin{aligned} a_x^n &= \frac{2}{L} + \int_0^L x(t).cos(\frac{2\pi nt}{L})\mathrm{d}t \\ a_y^n &= \frac{2}{L} + \int_0^L x(t).sin(\frac{2\pi nt}{L})\mathrm{d}t \ , \end{aligned} \tag{3.8}$$

and the contour was then reconstructed using only the first N Fourier coefficients that correspond to the lowest frequency components

$$\begin{aligned} x_s(t) &= a_x^0 + \sum_{n=1}^{N} a_x^{2n-1} cos(\frac{2\pi nt}{L}) + a_x^{2n} sen(\frac{2\pi nt}{L}) \\ y_s(t) &= a_y^0 + \sum_{n=1}^{N} a_y^{2n-1} cos(\frac{2\pi nt}{L}) + a_y^{2n} sen(\frac{2\pi nt}{L}) \ . \end{aligned} \tag{3.9}$$

We used $N = \frac{L}{f}$ to obtain the smoothed contour $c_s(t) = (x_s(t), y_s(t))$. Small details are more evident on contours with a small length, so the number of frequencies considered increases with respect to the contour length, being f the number of contour points used per frequency (refer to section 4.2). Based on the smoothed version, the concave points satisfy the inequality:

$$\|\overrightarrow{c_s^-(k)c_s(k)} \times \overrightarrow{c_s^-(k)c_s^+(k)}\| < 0, \tag{3.10}$$

where c^+ and c^- denote the previous and next contour point with respect to $c(k)$. Each set of connected concave points define a concave region. Figure 3.4 a) illustrates (in purple) the contour of $c(t)$ of a certain Ω_{ip}. The smoothed contour of $c(t)$ is illustrated in figure 3.4b) (in green). By comparing $c(t)$ and $c_s(t)$ it can be observed that the concave regions originated by small scale fluctuations and the discrete nature of $c(t)$ were eliminated.

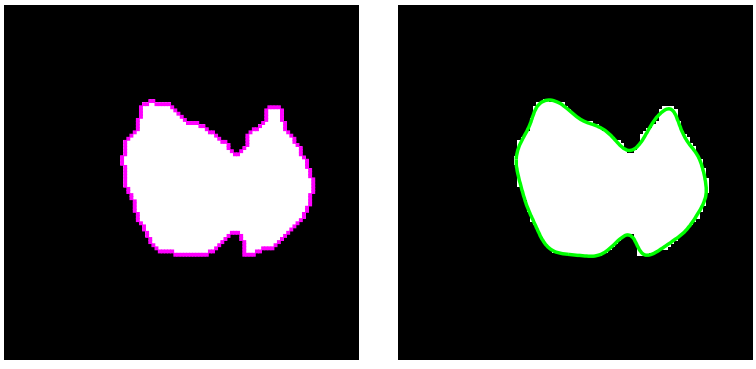

Figure 3.4: Cytoplasmic areas of a blob and its original and smoothed contour. Figure a) presents in purple the original contour of overlapping cytoplasms and figure b) presents in green the contour after smoothing.

We aimed to use the concave regions to perform the separation of overlapping cytoplasms, as we noticed that their intersection originates pairs of concave regions. Having observed that the boundary of two overlapping cytoplasms has a pair of concave regions, it was important to distinguish

between the genuine concavities and the spurious ones. The genuine concave regions were originated by cytoplasm overlapping and are hereinafter referred to as *true concavities*, whereas the concave regions originated by contour irregularities or noise are designated as *false concavities*. We proposed a separation of the overlapped cytoplasms based on the *true concavities* of the contour. The set of *true concavities* must be matched in pairs, so that a separation can be performed along the lines that link these pairs. Therefore, we proposed a matching process to determine the *true concavities* and perform their matching.

3.5 Matching Process

Firstly, the matching process must to distinguish between *true concavities* and *false concavities*. We noted that the *true concavities* often present a sharp concavity and this could be a discriminant feature to infer the nature of the concavity. Therefore, we defined the concavity of the n^{th} concave region as:

$$\psi(n) = \angle P_{n1}P_{n2}P_{n3}, \quad (3.11)$$

where P_{n1}, P_{n2} and P_{n3} are the initial point, the point with highest curvature and the final point of the n^{th} region, respectively. $\angle$ is the angle defined by three points. Regions with $\psi(n) > \Psi$ were considered as false concavities and were not matched, being Ψ is a pre-determined parameter in the range $[0, \pi]$ (refer to section 4.2). Although the remaining regions have $\psi(n) \leq \Psi$, they might not be *true concavities*. So, we aimed to match each one of the *true concavities* with the correct pair and left unmatched the *false concavities*. We used the alignment of concavities to perform the region matching. The alignment of the n^{th} region to the m^{th} region is given by

$$\alpha(n, m) = \angle \overrightarrow{v(n)}\ \overrightarrow{P_{n2}P_{m2}}, \quad (3.12)$$

where $\overrightarrow{v(n)}$ is the direction vector of the concavity defined as $\overrightarrow{v(n)} = \overrightarrow{P_{n1}P_{n2}} + \overrightarrow{P_{n3}P_{n2}}$. Figure 3.5 depicts the smoothed contour of overlapping cytoplasms in a ROI. The concave regions of the contour with $\psi(n)$ lower than Ψ are presented in red. The different features extracted are also marked for some regions. The blob that originated this ROI has its cytoplasm overlapped by two other cytoplasms. Their intersection originated the pairs $(1, 5)$ and $(2, 4)$ of concave regions.

The rationale of choosing pair alignments as a discriminant feature is evident in this example. Pairs of overlapping regions are most times aligned, i.e., $\alpha(n, m)$ and $\alpha(m, n) \approx 0$, therefore we concluded that the cost of associate the n^{th} region to the m^{th} region was proportional to $\alpha(n, m)$. Moreover, this cost was also proportional to $\psi(n)$, since the lower $\psi(n)$ the higher the likelihood of the n^{th} region be originated by overlapping cytoplasms. Therefore, let A be a set of concave regions, we defined the cost of matching the n^{th} region to the m^{th} region within A as

$$M_A(n, m) = w_1 \frac{\alpha(n, m)}{\pi} + w_2 \frac{\psi(n, m)}{\pi} + w_3 \frac{d(n, m)}{sup(d_A)}, \quad (3.13)$$

and the cost of the full match is given by

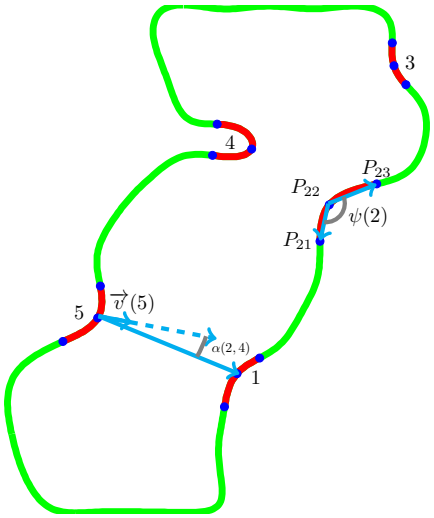

Figure 3.5: The main features involved in the matching process. The concave regions of the contour are marked in red and the three points that define each one of the features of a concave region are presented in dark blue.

region	1	2	3	4	5
1	-	0.53	0.57	0.47	0.47
2	0.57	-	0.58	0.34	0.49
3	0.54	0.50	-	0.40	0.49
4	0.38	0.19	0.27	-	0.49
5	0.35	0.46	0.54	0.52	-

Table 3.1: Example of the cost $M_A(n,m)$ involved in the region matching process.

region	1	2	3	4	5
1	-	0.55	0.55	0.43	0.41
2	-	-	0.54	0.26	0.48
3	-	-	-	0.33	0.52
4	-	-	-	-	0.51
5	-	-	-	-	-

Table 3.2: Example of the cost $\kappa_A(n,m)$ involved in the region matching process.

$$\kappa_A(n,m) = \frac{M_A(n,m) + M_A(m,n)}{2}, \quad (3.14)$$

where d_A is the set of all distances between two regions in A, w_n are the feature weights (in our experiments $[0.5, 0.4, 0.1]$).

Tables 3.1 and 3.2 present the costs values for the example illustrated in figure 3.5. We expected a inverse relation between the value of $\kappa_A(n,m)$ and the likely of the pair (n,m) be originated by cytoplasm intersection, therefore the correct pairs can be determined by the minimum values of κ. Based in this idea we performed the matching of the concave regions contained in A by finding a bijection $f : A \to A$ constrained to

$$min(\kappa_{A \setminus B}) = \kappa(a_n, f(a_n)) \wedge a_n \neq f(a_n), \ \forall n \in \{1, 2, ..., |A|\}, \quad (3.15)$$

where $B = \{a_1, a_2, ..., a_{n-1}\}$. We preferred this constraint rather than determining the set of pairs that minimizes the sum of κ, since it is more accurate in this type of problem. If the pairs were determined to minimize the sum of κ, then the values of κ for each pair would be balanced, whereas with our constraint the first pairs will correspond to the minimum values of κ, and the last pairs (composed by the remaining regions) may contain extreme values of κ. This can be useful to decide that maybe these pairs (the latter) are not genuine and these regions must not be matched. To exclude from f these spurious matches, the pairs with a cost higher than γ (refer to section 4.2) where not considered.

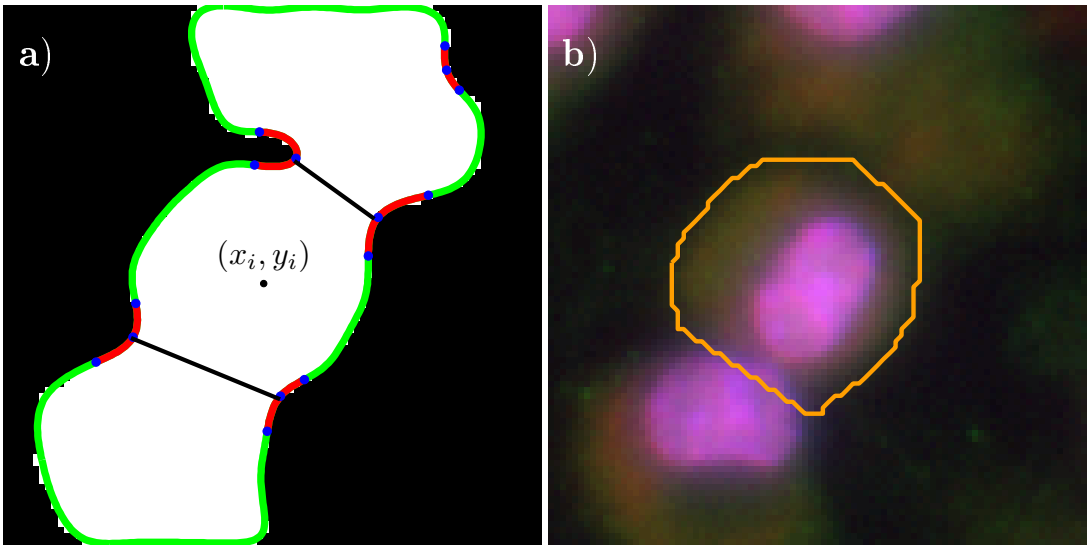

Figure 3.6: Part of a fluorescence image and the most important structures involved in the annotation of *Leishmania* infections. The use of fluorescence allows to visualize the macrophage nuclei as pink, the parasites as green and the cytoplasm of the macrophages in shades of red.

Once f is determined, a set of frontiers is built using the lines that are defined by the regions a and $f(a)$, for all a that belong to the domain of h. Figure 3.6a) illustrates this process for the example given in figure 3.5. The pairs of regions obtained from f are $(1, 5)$ and $(2, 4)$. The points with highest curvature of each of these regions were used to define the lines to link the regions and perform the separation of cytoplasms. After this process, the regions that do not contain (x_i, y_i) are not considered, yielding the final segmentation of the cytoplasm associated with the blob detected at (x_i, y_i), designated hereinafter as S_i. Figure 3.6b) illustrates the boundaries of S_i superimposed in the original ROI.

3.6 Refinement Process

Having observed frequent slight inaccuracies in our results, we carried out a refinement phase to determine if the cytoplasm segmentation is complete or not, and perform the necessary adjustments. The segmentation of the i^{th} blob is only considered complete if S_i is convex. We consider the contour of S_i convex when

$$\psi(n) > \Psi, \forall n \quad , \quad (3.16)$$

When the contour of S_i, yielded from the matching process, is convex the refinement is not required. In case of S_i be concave, we intend to ascertain the nature of concavities. Strong concavities can denote the existence of multiple cells in S_i, whereas concavities with low sharpness may be caused by shape irregularities. Therefore, we proposed to recall the matching process and lowering Ψ by $\frac{\pi}{12}$, at most twice. After this, it is expected that S_i is convex, otherwise the cytoplasm segmentation can not accepted. Consequently, the cytoplasm segmentation is discarded, but its corresponding blob location is preserved to feed association process. Although very uncommon, the rejection of cytoplasm can occur due to noise, shape irregularities, severe overlapping or the existence of only one concavity.
Amongst these cases, we observed the latter as the most common and we devoted a solution to this. Regions with only one concavity were often originated by two overlapping cytoplasms. In some cases one of the concavities is absent due to the way cytoplasms intersect or to their irregular shape. As these cases could not be solved by the matching phase, since there is not a corresponding pair for the concavity, we proposed a forced separation to handle correctly regions with one concavity. In this forced separation, the separation occurs throughout the line defined by the vector $\overrightarrow{v}(1)$. This choice was motivated by the fact that true pairs of concavities present a value of $\alpha(n, m)$ close to 0. This way $\overrightarrow{v}(1)$ will be an approximation of the vector that links the existing concavity to the absent one.

Figure 3.7 exemplifies a case where the segmentation would be considered incorrect without this refinement phase. The detected blob is overlapped by other cells, and our matching process was able to identify the correct pair of concavities that separates the cytoplasm of the desired blob from the others. However, after the separation, the contour of S_i remains with some concavities originated by the irregular shape of the cytoplasm. These false concavities (figure 3.7d), did not allow to consider S_i as convex, since their sharpness is lower than Ψ. After the first lowering, only one concavity remained (figure 3.7e), whereas the second lowering allows to consider the contour convex, since there are any concavity with a sharpness lower than Ψ (figure 3.7f).

3.7 Association Process

In this phase it is expected S_i to be convex. As mentioned before, this can occur immediately after the matching process or only after the refinement process. Since convex contours are highly likely to contain only one cell, the region of S_i can be considered as belonging to the i^{th} blob. Based on this idea, we aim to associate the region comprised by S_i to the i^{th} blob, so that any other cytoplasm or nucleus can intersect with this region. This implies that multiple detections contained in S_i are removed. Besides, further segmentations can never contain any part of S_i. With this, we ensure that cytoplasms do not intersect, and thus each parasite is assigned to one macrophage at most.

3.8 Correction Process

This phase is motivated by an image property - parasite nucleus visibility in red channel - that we consider useful to verify if the blob detection and the cytoplasm segmentation steps have underestimated the number of parasites. Due to their reduced size in the images, it is common that these two phases consider the existence of only one parasite where two or more actually exist. This can also happen to parasitologists, but they consult the red channel to correct their first

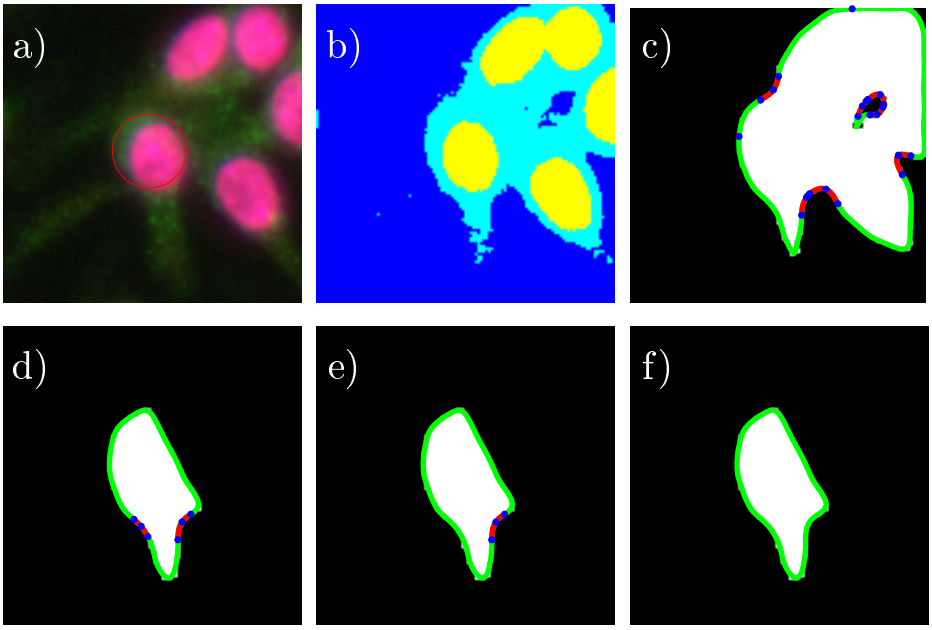

Figure 3.7: Example of a case where the cytoplasm segmentation would fail without the refinement phase. a) ROI gathered for a detected blob. b) Clustered ROI. c) Smoothed contour and the concavities considered by the matching process. d) Results obtained after the separation of overlapping cytoplasms and the concavities present in the smoothed contour with a sharpness lower than Ψ. e) and f) The concavities considered after lowering Ψ by $\frac{\pi}{12}$ and $2\frac{\pi}{12}$, respectively.

guess. Therefore, we also adopted this strategy, and the parasite processing is complemented with a correction process.

In this phase we inspect the area comprised by parasite cytoplasm, in order to verify the existence of multiple nuclei in these regions. For this, we used blob detection in the red channel and remove the detections that lie outside the parasites cytoplasms previously segmented. This way, cytoplasms containing more than one detection will be divided, what improves the system performance by avoiding underestimation.

Chapter 4

Results and Discussion

4.1 Materials

4.1.1 CellNote

The CellNote software developed by Bruno *et* al. [Lop10] provide to parasitologists a more interactive and credible way to perform cell counts [LCC+13]. Graphical marks, usually designated as annotations, are used to identify the presence of a certain cell in a position of the image. Figure 4.1 illustrates the CellNote software, with an image of *Leishmania* infections partially annotated.

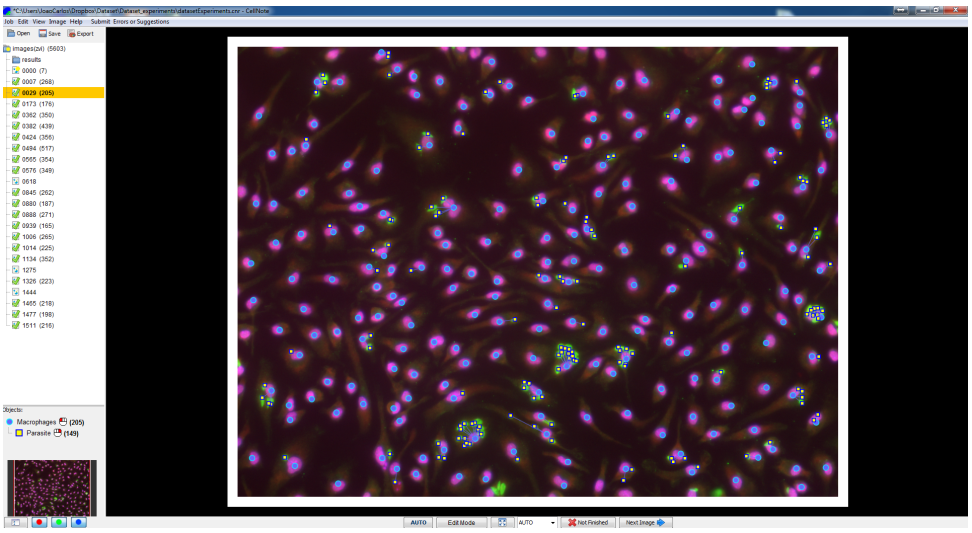

Figure 4.1: The CellNote software.

4.1.2 Dataset

In this work, we have established a partnership with the *Instituto de Biologia Molecular e Celular* (IBMC), that provided us a set of fluorescence images with *Leishmania*-infected macrophages. Those images were acquired with the AxioImager Z1 microscope using fluorescence. Each image was annotated by one parasitologist using CellNote software. As the annotation toughness differs amongst images - mainly due to parasite clustering and image quality - we have proposed a four category classification :

Table 4.1: The four categories proposed to classify the toughness of annotation.

		Parasite clustering	
		Low	High
Image Quality	Good	1	2
	Bad	3	4

Having noticed that the set of images provided was not uniformly distributed for the categories considered, we have built a dataset composed by 140 images, representing the most common cases in *Leishmania* infections. To construct a fair dataset, each one of the four categories was evenly represented.

4.1.3 Data correction

To perform the development, optimization and test of our approach we relied on the built dataset to gather images. Since the annotation performed by humans is not error free and the positions marked may not lie inside the cellular data we carried out a cross-verification, i.e., the positions of every manual annotation were adjusted to lie in the centroid of the cells. This is important to ensure the performance of the system is correctly assessed, once the way we assessed the performance depends on the manual annotation positions.

4.1.4 Performance evaluation

Let the corrected manual annotations be denoted by $M_{man}(i)$ (macrophages) and $P_{man}(i)$ (parasites). Let the output of the automated methods be denoted by $M_{aut}(i)$ and $P_{aut}(i)$. The performance was assessed by counting the number of automatic annotations that were correctly assigned. As it is almost impossible that both manual and automatic annotations for a given instance are placed at the exact same location, a more flexible performance evaluation rule was devised. The *cost* of assigning an annotation P_i to P_j was considered as the Euclidean distance between P_i and P_j, such that $C : P_{aut} \times P_{man} \rightarrow \mathbb{R}$. The goal is to determine a function $h : A \rightarrow B$ such that $\sum_{n \in A} C(n, h(n))$ and $|B|$ is minimized, constrained by $C(n, h(n)) < r,\ \forall n \in A\ .\ |.|$ denotes the cardinality of a set. A and B are partitions of P_{aut} such that $A = \{a \in P_{aut} : h(a) \neq \emptyset\}$ and $B = \{b \in P_{aut} : h(b) = \emptyset\}$. This was regarded as a linear assignment problem, and the Hungarian Algorithm[KY55] used to solve it. The true positives (TP), the false positives (FP) and the false negatives (FN) are given by $TP = |A|$, $FP = |B|$, $FN = |P_{man} \setminus Img(h)|$. The cellular data that lies in the borders are not considered by the parasitologists, since they are not completely visible and may be misleading. We observed that the lack of annotations in these regions was a frequent source of error for all techniques evaluated. Therefore, we have discarded from the domain and co-domain of h all the annotations contained in the image borders, as exemplified in figure 4.2.

4.2 Performance Optimization

In the chapter 3 we stated that some phases of the proposed method depend on pre-determined parameters. As the optimal values for these parameters may vary for different types of images, we used fifteen images (containing more than 4 000 macrophages and almost 4 500 parasites) to infer the values that maximize the performance of our system in images with *Leishmania* infections. The system performance was measured using the harmonic mean between precision and recall, usually denoted as F-measure. The domain of each parameter was divided in equally-spaced intervals to determine the F-measure of the system along each value.
Figure 4.3 depicts the system performance with respect to the value of each parameter in macrophage and parasite detection. Moreover, the tests were conducted using two clustering algorithms, the K-means (in green) and a multi-level threshold algorithm[LCC01] (in red). The results were observed to be highly similar, even though the K-means was selected due to its slightly better performance. This experiment allowed us to observe how system performance varies according to each parameter.

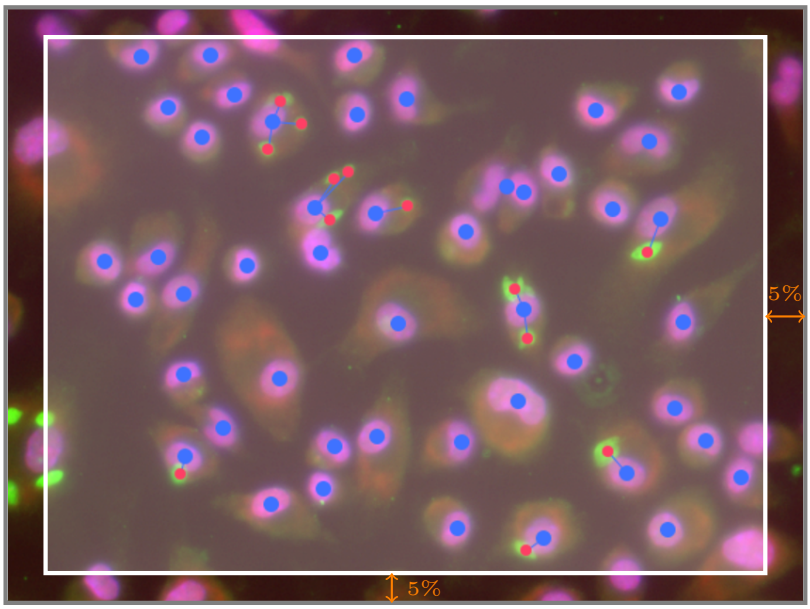

Figure 4.2: Example of the region considered for performance evaluation. The manual and automatic annotations that lie in the image borders are removed from f.

It is interesting to note that ε is the only parameter that causes an extreme variation on F-measure. Blob detection is filtered by ε, so very low performance is expected when ε is high, as almost every blob is removed. However the reverse is not true, as the lower ε the higher the amount of blobs accepted, including the spurious ones. In fact, F-measure achieves its maximum at $\varepsilon = 0.15$ and $\varepsilon = 0.2$ for macrophages and parasites, respectively.

Table 4.2: Optimal values for each one of the pre-defined parameters of our approach, according to a training data set of fifteen images.

	ε	f	Kc	Ψ	γ
Macrophages	0.15	14	3	$\frac{11}{12}\pi$	0.55
Parasites	0.2	12	3	$\frac{11}{12}\pi$	0.65

In what concerns f, we observed that F-measure decreases as f moves toward 0 or as f moves toward $+\infty$, achieving its maximum at $f = 14$ and $f = 12$ for macrophages and parasites, respectively. As the number of Fourier coefficients used in contour smoothing phase is inversely proportional to f, low and high values of f will lead to contours with too much and too few details, respectively. Consequently, *true concavities* begin to fade away as f increases and *false concavities* are not properly removed as f decreases. This explains why system performance is maximized for middle values of f.

In regard to Kc, is clear that three clusters are the best solution for macrophages and parasites. In order to explain these results we have inspected the general distribution of images intensity. Although in the majority of the cases a bi-modal distribution (background and cells) was observed, we concluded that two clusters would associate the darkest parts of cytoplasm with background, and the brighter parts with the foreground, yielding a incorrect segmentation of cytoplasm. An additional cluster solves this problem, whereas a high number of clusters would split cytoplasm in

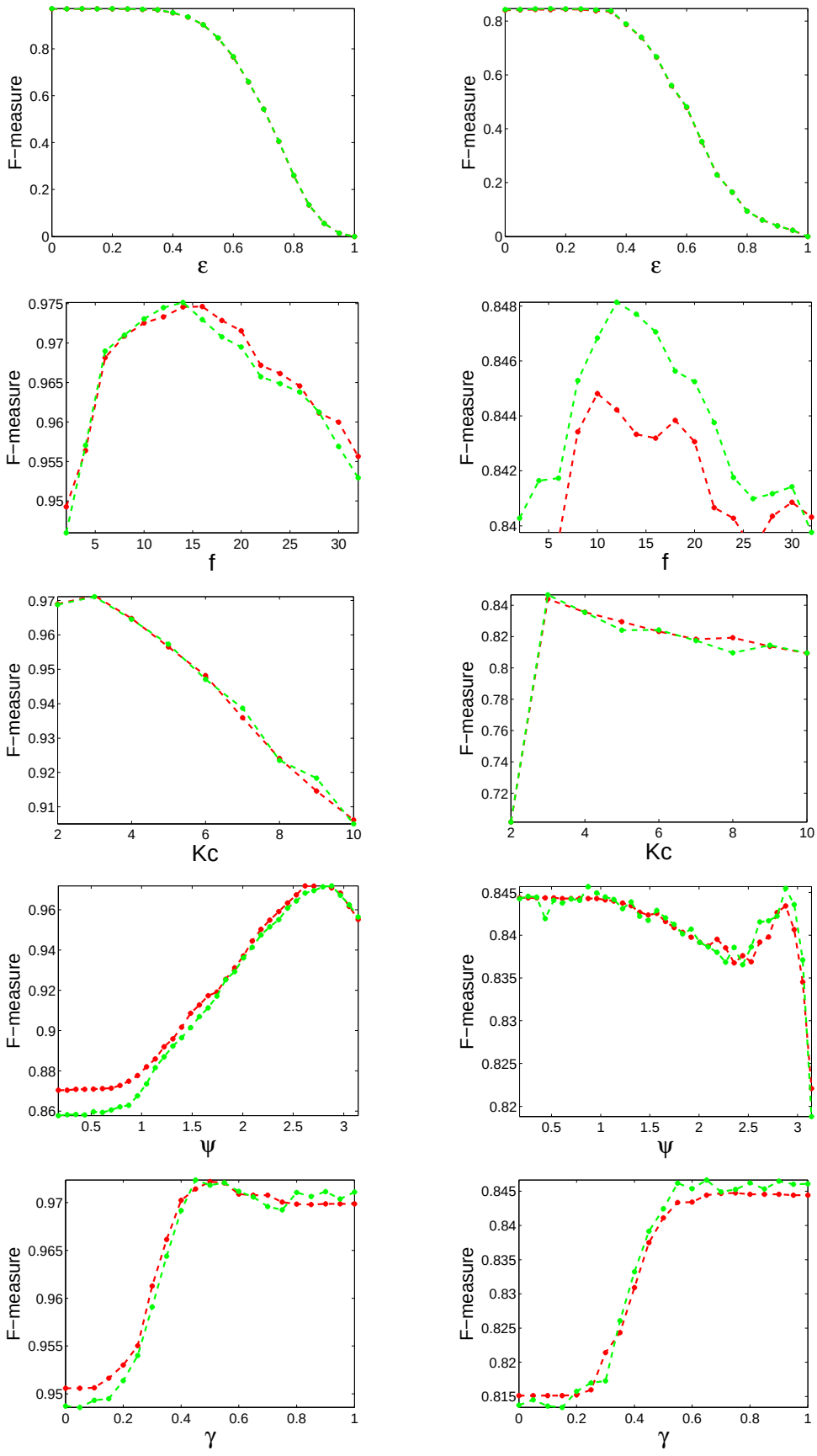

Figure 4.3: Results obtained in the detection of macrophages (left column) and parasites (right column), with respect to values of the most important parameters. Results are given for two different clustering algorithms (green lines correspond to k-means and red lines to a multi-level multi-level threshold algorithm).

different clusters.
In the Ψ graphics it can be observed how the system would perform if the matching phase did not exist, i.e. when $\Psi = 0$ all concavities are considered as spurious and no matching is performed. Additionally, every contour is considered as convex, what implies discarding a great amount of detections, since separation of overlapped cells is not performed and only one detection is maintained (as explained in section 3.7). We expected a directly proportional relation between Ψ and F-measure, however this was only observed in macrophages. This can be explained by the correction phase carried out in parasites processing. It is evident that in macrophage processing low values of Ψ erase *true concavities*, what restrains separation and, consequently, underestimates the number cells present. In fact, the same occurs in the parasites processing, yet the correction phase offsets the separations missed in matching phase.
At last, based on the relation between F-measure and γ can be observed how the system perform exclusively based in blob detection, i.e. when $\gamma = 0$ all the concavities paired by the matching process are rejected. The contour of overlapped cells will never be considered convex and the refinement phase will only yield the blob detections. As γ increases the number of rejected pairs decreases and more separations are performed, what increased the F-measure. However, this relation is not monotonic, F-measure achieves its maximum at $\gamma = 0.55$ and $\gamma = 0.65$ for macrophages and parasites, respectively. High values of γ do not prune all the incorrect pairs, yielding incorrect separations that can turn into under-segmentation or over-segmentation of the cytoplasm. In case of under-segmentation, the segmentation of macrophages cytoplasm will be incomplete, leading to an incorrect association between macrophages and parasites, and consequently, wrong estimation of infection levels. Although this is not mirrored by F-measure, the consequences of over-segmentation are. Over-segmentation is responsible for underestimation of macrophages and parasites, what explains the decline of F-measure as γ reaches 0. Table 4.2 contains the values chosen based on the obtained results (figure 4.3).

4.3 Discussion

In this section we explain some of the important choices carried out throughout the developing of our method and the adjustments performed to deal with some specificities of *Leishmania* infections. In addiction, we compare the advantages and drawbacks of our method with other approaches. We selected the methods of Leal *et* al. [LFM+12] and Nogueira [Nog11] for comparison purposes, based on the fact of being specialized in the particular type of images we aimed to work with. For both cases, the used implementations were supplied by the original authors.

4.3.1 Cytoplasm importance

In this work the ultimate goal is to detect the position of macrophages and parasites and establish a correspondence between them. Even though the segmentation of the cytoplasm is not demanded, we find that it useful to corroborate the detections obtained from the blob detection phase and to perform an association between macrophages and parasites in a more accurate way. Two illustrative cases are shown in figure 4.4 and 4.5.
Even though two nuclei are visible in figure 4.4a, a more careful analysis reveals the presence of one macrophage, as only one cytoplasm exists. An approach based only on blob detection would have failed. However, cytoplasm segmentation can overcome this issue, as shown by the results of our approach, given in figures 4.4b, 4.4c and 4.4d. After the clustering phase (figure 4.4b), the cytoplasmic areas are completely visible (light blue regions), and their shape suggest

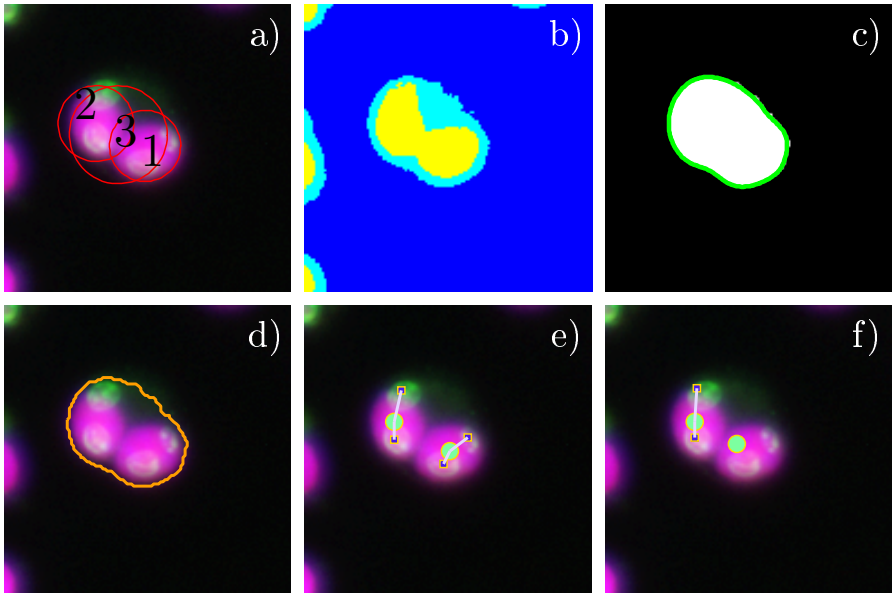

Figure 4.4: Illustrative case of the importance of cytoplasm segmentation to avoid excessive detection. a-d) Some phases our approach. e) Results obtained with Leal *et* al.'s approach. f) Results obtained with Nogueira's approach.

the presence of only one cytoplasm, as there are not strong concavities that evidence the existence of overlapping. The cytoplasmic areas associated with the 1^{st} blob and its smoothed contour are shown in figure 4.4c. Although a few concavities are evident in the smoothed contour, these are false concavities, mainly due to their low sharpness. The proposed matching process was able to correctly classify all the concavities as false concavities and therefore the separation was not performed. The cytoplasm boundaries associated with the 1^{st} blob are presented in figure 4.4d. As the contour yielded from the matching process was convex, the refinement phase was not required. The association process determined the region S_i as belonging to the cytoplasm of the nucleus detected by the 1^{st} blob. Additionally, this phase cleared the 2^{nd} and 3^{rd} blobs, once they lie inside S_1. For comparison purposes, figures 4.4e and 4.4f present the results obtained by the approaches of Leal *et* al.[LFM+12] and Nogueira[Nog11], respectively. Contrarily to our approach these approaches were not able to solve this case correctly, since the detections were only based on nucleus, yielding both two cells.

On the other hand, there are a few cases when the use of the cytoplasm might provide an incorrect segmentation, and an incorrect detection. Figure 4.5 illustrates one of these cases: noise between the two nuclei misled the clustering phase and both macrophages were segmented as a single cell (figure 4.5d). Unlike our solution, the methodologies of Leal *et* al. and Nogueira, presented in figures 4.5e and 4.5f, respectively, were able to solve this case correctly.

As the number of cases in which the cytoplasm segmentation provides incorrect results is much smaller than the ones where is useful, we concluded that cytoplasm segmentation turns out to be an advantage. This advantage is evidenced by the results provided in section 4.4.

Concerning the association between macrophages and parasites, the cytoplasm is also useful. The approach of Nogueira did not use the cytoplasm to determine which parasites are infecting each macrophage. Instead, the parasites were assigned to the nearest macrophage, based in the idea that a parasite is more close to the macrophage that is infecting than to the remaining macrophages. Although, this is correct in the majority of cases it fails in some of them, what degrades the estimate

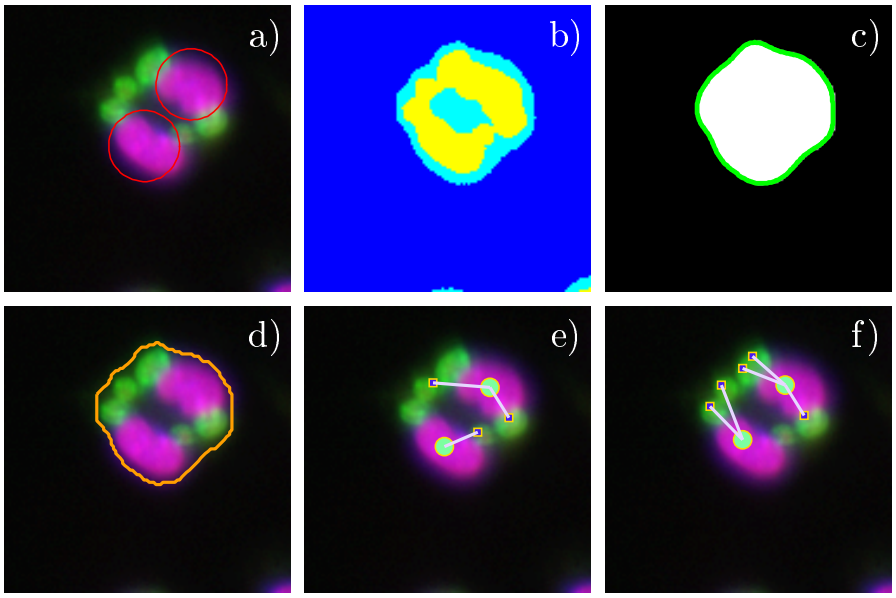

Figure 4.5: Illustrative case of cytoplasm segmentation drawbacks. a-d) Some phases our approach. e) Results obtained with Leal *et* al.'s approach. f) Results obtained with Nogueira's approach.

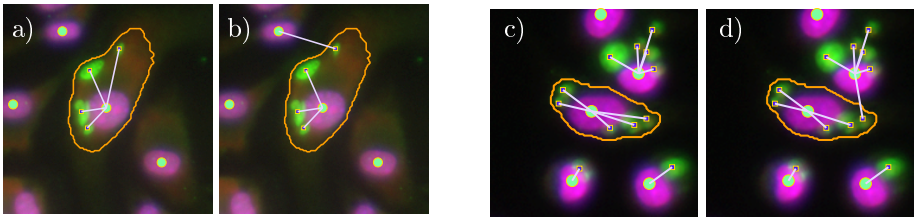

Figure 4.6: Two illustrative cases of cytoplasm segmentation importance to ensure a correct association between macrophages and parasites.

of PI and NPI. Figures 4.6b and 4.6d illustrate the associations obtained when the parasites are associated with the nearest macrophage, whereas in figures 4.6a and 4.6c the cytoplasm of the macrophage is used to check what parasites are contained and only next perform the associations. These are two examples when the cytoplasm is essential to obtain a correct association between macrophages and parasites.

4.3.2 Matching process

The matching process is a fundamental step of our approach. It performs better when the overlapping is not very severe. When the objects are very close, the separation may not be possible, as some important concave regions will be absent. As such, we included the concave regions present in the holes of B_{ic}. Figure 4.7 illustrates an example where a hole is present in B_{ic}. The use of concave regions of the hole are essential to achieve a correct segmentation of the cytoplasm associated with the 18^{th} blob.

As explained in section 3.6, the existence of only one concavity is the most common reason to restrain the success of the refinement phase in considering the contour convex. Figure 4.8 illustrates one of these cases. Our matching process was not able to solve this problem correctly, as the concave

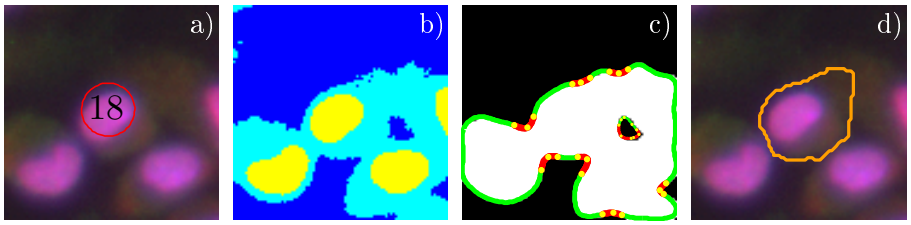

Figure 4.7: Illustrative case where the importance of using hole contour is evidenced.

region has not a pair to be matched. However, this was handled by the forced separation phase in our refinement process. Figure 4.8d) illustrates the results obtained with the forced separation step using the only true concave region of the contour.

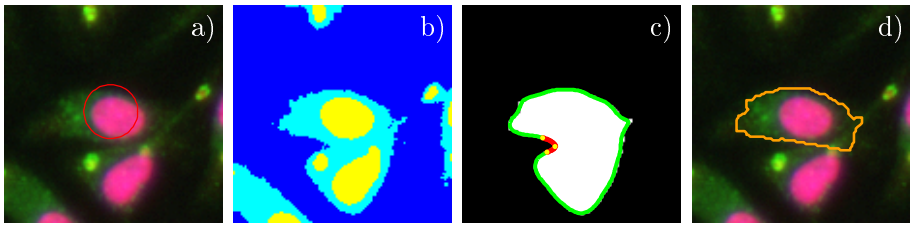

Figure 4.8: Illustrative case where forced separation is essential to yield a correct result.

4.3.3 Parasites nuclei importance

In detecting parasites, the segmentation of the cytoplasm is complemented by the detection of parasites nuclei carried out by the correction process. They are not always visible, due to their dimension. However, when they are present it is important to detect them, in order to ensure that the segmented cytoplasm corresponds to a single parasite. Figure 4.9 regards one case where the detection fails if the parasite nucleus was not used. Our approach were only able to detect one blob in a region where actually two parasites exist (figure 4.9a). Besides, the separation phase considered the parasites as a single cytoplasm. The blob detection performed after the cytoplasm segmentation allowed us to rectify this cases, as shown in figure 4.9d.

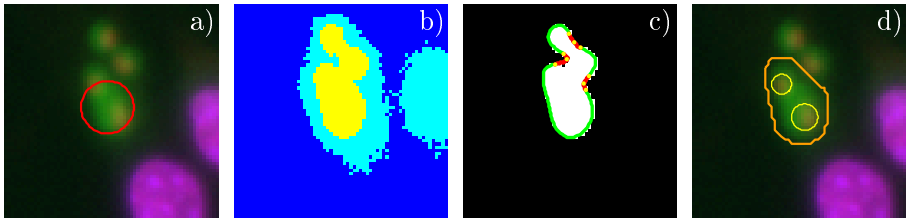

Figure 4.9: Most notorious cases, illustrating the advantages and drawbacks of our approach when compared with the other methods.

4.4 Results

In this chapter the key points are two-fold: 1) Analyse the performance of our approach regarding the used measures of interest; 2) Compare our results with the performance of other approaches.

Regarding the first issue we have performed two types analysis: At first, we aimed to compare the numerical predictions of our approach with the ground truth. For this purpose we carried out tests in a set of manually annotated images, yielding table A.1. In order to objectively measure how much our method deviates from the ground truth we have used Δ_p :

$$\Delta_p = \frac{p_{aut} - p_{man}}{p_{man}}, \quad (4.1)$$

being p one measure that can be inferred by the image analysis. Δ_p gives the percentage difference between our method and the manual annotation, providing a fairer comparison between the two approaches than a simple difference. Δ_p allows to describe how close the automatic approach is from the ground truth, but does not consider if the automatic annotations were correctly assigned. Therefore, we accomplished a deeper analysis of our approach by inspecting the detection error on macrophage and parasites process, yielding table A.2.

Concerning the second issue we carried out a performance comparison with Leal *et* al. and Nogueira methods due to the reasons explained in section 4.3.

Table 4.3: The mean values of Δ_p and $|\Delta_p|$ for each one of the measures presented in the table A.1

		$\#M$	$\#P$	$\#IM$	PI	NPI	II
Our approach	$\overline{\Delta_p}$	-1.1%	-6.6%	-2.2%	-1.2%	-5.3%	-5.8%
	$\overline{\lvert\Delta_p\rvert}$	2.3%	18.8%	10.4%	10%	13.9%	18.5%
Leal *et* al.'s approach	$\overline{\Delta_p}$	5.1%	5.2%	22.6%	17.2%	-14.7%	0.4%
	$\overline{\lvert\Delta_p\rvert}$	5.2%	22.1%	23.0%	20.3%	16.3%	22.1%
Nogueira's approach	$\overline{\Delta_p}$	-4.1%	-1.6%	-8.2%	-1.7%	7.8%	8.9%
	$\overline{\lvert\Delta_p\rvert}$	11.6%	23.2%	16.1%	15.3%	19.1%	29.2%

In order to summarize the information contained in table A.1, we determined the mean value of Δ_p and $|\Delta_p|$ for the number of macrophages(#M), the number of parasites(#P), the number of infected macrophages(#IM), Percentage of Infection (PI), the mean Number of Parasites per Infected cell (NPI) and the Infection indeX (IX). This information is given in table 4.3 and the results are discussed in the next subsections. Moreover, we also present the performance of macrophage and parasite detection in table 4.4, together with the results obtained by the tested approaches.

All the results given in this section regard 24 images gathered from our dataset. It should be noted that all these images are disjoint of the data used either during the development and optimization of the proposed method. Even though the number of images used might be - at a glance - considered short, it should be stressed that it contains about 6 500 macrophages and almost 7 000 parasites.

Table 4.4: Comparison between the results obtained by our approach and two previously published methods. Precision, recall and F-measure values are given with the corresponding 95% confidence intervals.

	Macrophages			Parasites		
Method	**Precision(%)**	**Recall(%)**	**F-measure(%)**	**Precision(%)**	**Recall(%)**	**F-measure(%)**
Leal	94.30 ± 0.61	99.63 ± 0.04	96.89 ± 0.37	79.66 ± 1.61	82.45 ±1.02	81.03 ±1.17
Nogueira	93.25 ± 0.34	88.52 ± 1.41	90.82 ± 1.04	78.79 ± 1.51	77.75 ± 1.26	78.27 ±1.12
Joao	98.19 ± 0.18	97.18 ± 0.11	97.68 ± 0.09	81.57 ± 1.09	87.61 ± 0.93	84.48 ±0.60

4.4.1 Number of Macrophages

The analysis of table A.1 reveals little difference between the number of macrophages (#M) found by our method and the number of macrophages found manually, what is evidenced by $\overline{|\Delta_{\#M}|} = 2.3\%$. From the observation of figure 4.10 we can conclude that in 95% of the cases it is expected that, in average, the number of macrophages predicted by our approach deviates between 1.7% and 2.9% from the correct number of macrophages in the image.

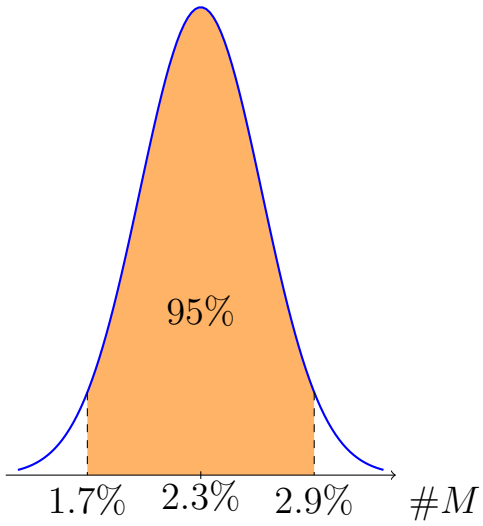

Figure 4.10: Probability density function of $|\Delta_{\#M}|$ assuming a normal distribution. The bounds for the 95% confidence interval are also presented.

By observing $\overline{\Delta_{\#M}} = -1.1\%$ we conclude that the automatic approach tends to underestimate the number of macrophages present. This is corroborated by the precision and recall of macrophage detection, since recall is lower than precision, and consequently, the amount of FN is higher than FP. These results are mainly due to our cytoplasm segmentation phase. As explained in subsection 4.3.1, the segmentation of the cytoplasm constitutes an effective way to correctly classify macrophages with multiple nuclei, but implies a slight increment in the amount of FN. However this decrement in Recall is offset by the improvement of Precision, as evidenced by the F-measure achieved by the three approaches in table 4.4.

4.4.2 Number of Parasites

Regarding the number of parasites (#P), table A.1 evidences some cases with significant differences between automatic and manual approaches. In average, our approach underestimates the number of parasites present in a image, since $\overline{\Delta_{\#P}} = -6.6\%$. Assuming that $\overline{|\Delta_{\#P}|}$ follows a normal distribution, it can be expected that the deviation between automatic and manual approaches lies in the interval $[12.1\%, 25.4\%]$ with an average of 18.8%, figure 4.11. A deeper analysis of parasite detection reveals a Precision and Recall of 81.6% and 87.6%, respectively.

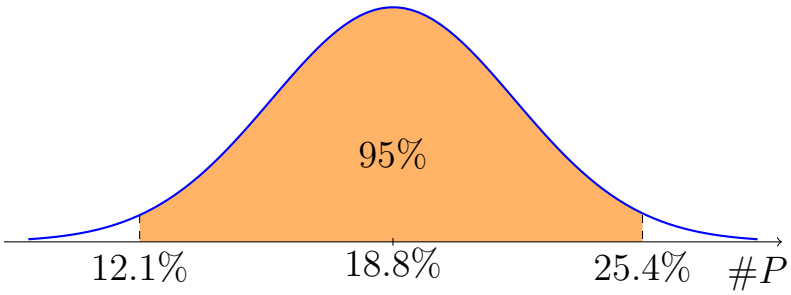

Figure 4.11: Probability density function of $|\Delta_{\#P}|$ assuming a normal distribution. The bounds for the 95% confidence interval are also presented.

It is clear that the performance is poorer in parasite annotation, what can be explained by the difficulty and subjectivity of this task. Due to the magnification used in our type of images, parasites are reduced in size. Therefore, clusters of parasites are harder to count, increasing the subjectivity of the task. Thus, manual annotation has significant differences between different parasitologists, allowing our results to be considered acceptable. Besides, our parasite process is considered an improvement when compared to the other two automatic approaches, as evidenced by the F-measure in table 4.4.

4.4.3 Number of Infected Macrophages

The number of infected macrophages (#IM) constitutes a crucial property of the image, since it determines PI and NPI. As discussed in the subsection 4.3.1, the segmentation of the cytoplasm is useful to provide a correct association between macrophages and parasites, and consequently, obtain a more accurate estimation of #IM. This explains why, in average, our approach presents a lower $|\Delta_{\#IM}|$ than Nogueira's method (see table 4.3). This difference is also due to our improvement in parasite detection, what is evidenced by the results of Leal's approach for $|\Delta_{\#IM}|$.
With the results obtained, we can assure that in 95% of the cases the deviation from the manual approach is higher than 6.4% and lower than 14.4%.

4.4.4 PI

The percentage of infection (PI) represents one of three measures used by parasitologists to draw conclusions about the capacity of *Leishmania* to survive/replicate under the effect of certain drugs. Inferring these measures is the main goal when annotation is carried out, rather than determine the parasites and macrophages locations. However, this is greatly dependent on the correct detection and association of macrophages and parasites, justifying our focus on the accuracy of detection.
PI is determined by the quotient between #IM and #M, therefore it is expected a correlation between the results achieved for these two measures and PI. This is corroborated by the similarity between $|\Delta_{PI}|$ and $|\Delta_{\#IM}|$, mainly ensured by the good results accomplished in macrophages

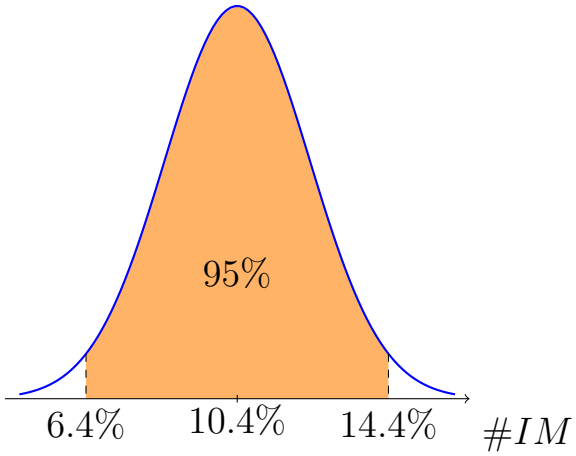

Figure 4.12: Probability density function of $|\Delta_{\#IM}|$ assuming a normal distribution. The bounds for the 95% confidence interval are also presented.

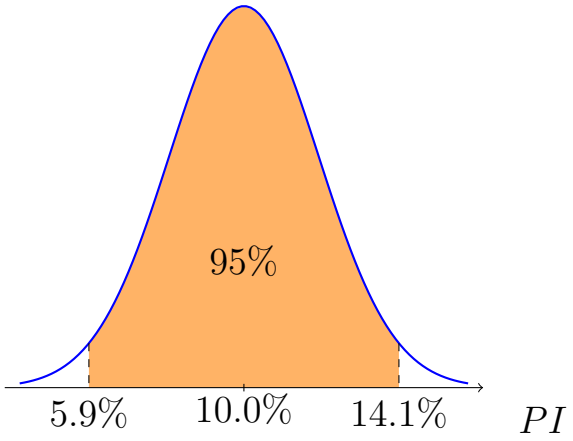

Figure 4.13: Probability density function of $|\Delta_{PI}|$ assuming a normal distribution. The bounds for the 95% confidence interval are also presented.

detection, that prevented the degradation of $|\Delta_{PI}|$. Results evidence a deviation between 5.9% and 14.1% from the manual approach, when using our method to automatic evaluate PI.

4.4.5 NPI

The number of parasites per infected macrophage (NPI) is another measure of interest to parasitologists. According to its definition, given in subsection 2.1.4, it depends on the performance of parasites detection and #IM.

On average, our approach deviates of 13.9% from the correct value of NPI, being assured that the true value of $|\Delta_{NPI}|$ lies in interval $[10.2\%, 17.6\%]$ for a confidence of 95%.

When compared with the evaluation of #P, results obtained for NPI are more accurate. Since the number of parasites and infected macrophages is underestimated by our method ($\Delta_{\#P} < 0$ and $\Delta_{\#IM} < 0$) evidence this), the quotient between these two measures has a lower deviation from the correct value of NPI.

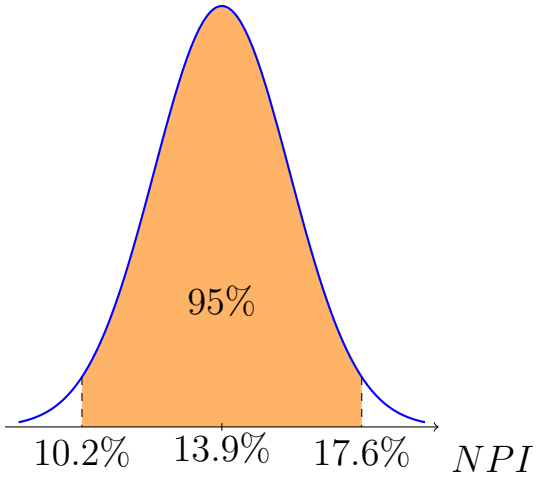

Figure 4.14: Probability density function of $|\Delta_{NPI}|$ assuming a normal distribution. The bounds for the 95% confidence interval are also presented.

4.4.6 Infection Index

The Infection indeX (IX) is determined by the product of PI and NPI, and, measures the number of parasites per macrophages.

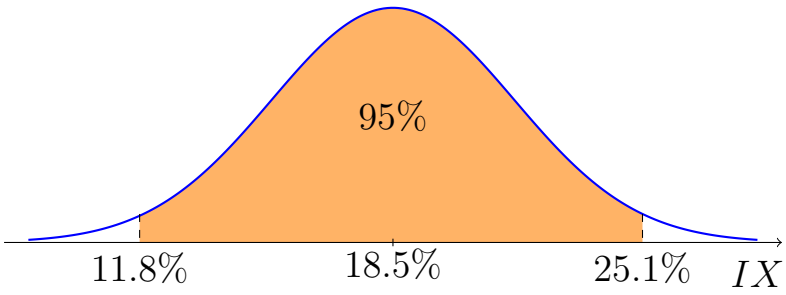

Figure 4.15: Probability density function of $|\Delta_{IX}|$ assuming a normal distribution. The bounds for the 95% confidence interval are also presented.

The Infection index determined the by our automatic approach deviates, on average, 18.5% from manual evaluation. For a confidence of 95%, it is expected the true value of Δ_{IX} to be comprised in the interval $[11.8\%, 25.1\%]$ The results achieved for this measure are similar with the ones achieved for #P. As in the case of PI, the similarity between the results accomplished for IX and #P is explained by the good accuracy of macrophage detection.

4.4.7 Performance comparison

In summary, the general observation of the results yields two conclusions: 1) In average, our approach tends to underestimate the correct values of each measure of interest. On the contrary, Leal *et* al.'s approach tends overestimate to these measures, whereas Nogueira's method does not present a clear trend. 2) Regarding the absolute deviation between automatic and manual data, our approach has achieved the best results in every measure.
Firstly, the differences can be explained by the strategy adopted in our approach. As explained in 4.3.1, we have developed strategies to handle correctly polynuclear cells, what in some cases can underestimate the number of correct detections. Inversely, an approach based only in blob

detection is prone to overestimation due to incorrect detection of polynuclear cells. The results yielded by Leal *et* al. approach evidence this conclusion.
Secondly, the deviation from manual annotation has decreased in every measure, when compared to the other two approaches. This was positively regarded and considered as the main achievement of the research work. Furthermore, this is also corroborated by the F-measure of our system, table 4.4.

Chapter 5

Conclusion

In this work, our main goal was the development of a method to perform the annotation of fluorescence images with Leishmania-infected macrophages in a reliable way. Such method constitutes an asset for parasitologists for two major reasons: 1) Releases parasitologists from the time-consuming manual annotation, speeding up their research work. 2) Withdraws subjectivity from the annotation process, commonly experienced in these type of images.

Two other approaches were previously proposed for this problem, but the challenges in fluorescence images with Leishmania-infected macrophages restrained their performances, mainly in parasite detection. Having this in mind, we have also focused on improving these performances by analysing their main drawbacks and weakness.

To achieve such goals, we have concluded that, although not required, the segmentation of the cytoplasm can be very effective in the correct detection of polynuclear cells, as well as, in the association between macrophages and parasites. Besides, we have noticed the ineffectiveness of common segmentation techniques such as watershed or region growing, since they exploit the fact that the intensity of fluorescence-stained cells usually decreases from the core to the boundary, which is not confirmed in our type of images. To solve this problem we focused on contour analysis and have based our approach on the contour convexity, in order to decide if a region should be segmented as a single cell. This way, we have improved macrophage detection performance by avoiding errors introduced by nuclei detection. Regarding parasites processing, we have concluded that the typical detection by cytoplasm in the green channel could be improved by combining these results with nuclei detection in red channel.

These conclusions are evidenced in section 4.4, where a performance comparison between the three approaches reveals an improvement in what regards macrophage and parasite detection. Parasitologists' opinions to the results obtained by our approach are also favourable. They referred being highly confident in our macrophage detection, whereas the parasite detection results were considered acceptable.

In conclusion, the investigation carried out in this work enabled the development of a method able to automtically annotate *Leishmania* infections. Furthermore, when compared to similar approaches, experimental results confirm our system as an improvement. Therefore, we consider all our goals fulfilled.

5.1 Contributions and Achievements

The main contribution of our work is a functional method able to automatically annotate fluorescence images with *Leishmania*-infected macrophages. The results attained by our approach can also be considered an achievement, since they outperform the performances obtained by methods previously proposed to perform annotation of *Leishmania* infections. Additionally, the work described in this thesis has been summarized in a conference paper[NCPC13], already accepted for publication in International Conference on Image Analysis and Recognition (ICIAR) 2013.

5.2 Future Work

At the present time, we have integrated our system in CellNote software as a plug-in. Parasitologists from Institute for Molecular and Cell Biology (IBMC) are testing our approach in new images obtained from their experiments with *Leishmania* infections. Based on their feedback, we expect continuing the improvement of our method, mainly in parasite detection.
In addiction, we are also interested in extending our work so that it can be adapted to counting of other type of cellular data. We consider our matching process flexible enough to provide a general solution for splitting overlapped cells (the main reason for performance degrading). To provide experimental support for these statements we plan to test some phases of our approach in images with different types of cells, where counting is required.

Bibliography

[AB94] R. Adams and L. Bischof. Seeded region growing. *IEEE Trans. Pattern Anal. Mach. Intell.*, 16(6):641–647, June 1994. 16

[BL79] S. Beucher and C. Lantuejoul. Use of Watersheds in Contour Detection. In *International Workshop on Image Processing: Real-time Edge and Motion Detection/Estimation, Rennes, France.*, September 1979. 17

[BMP02] S. Belongie, J. Malik, and J. Puzicha. Shape matching and object recognition using shape contexts. *IEEE Trans. Pattern Anal. Mach. Intell.*, 24(4):509–522, April 2002. 20

[BSZ09] Xiangzhi Bai, Changming Sun, and Fugen Zhou. Splitting touching cells based on concave points and ellipse fitting. *Pattern Recognition*, 42(11):2434 – 2446, 2009. 22

[Can86] John Canny. A computational approach to edge detection. *Pattern Analysis and Machine Intelligence, IEEE Transactions on*, PAMI-8(6):679 –698, nov. 1986. 13

[CSS+02] Helena Castro, Carla Sousa, Marta Santos, Anabela Cordeiro da Silva, Leopold Floh'e, and Ana M Tom'as. Complementary antioxidant defense by cytoplasmic and mitochondrial peroxiredoxins in leishmania infantum. *Free Radical Biology and Medicine*, 33(11):1552 – 1562, 2002. 4

[CV95] Corinna Cortes and Vladimir Vapnik. Support-vector networks. In *Machine Learning*, pages 273–297, 1995. 21

[DH72] Richard O. Duda and Peter E. Hart. Use of the hough transformation to detect lines and curves in pictures. *Commun. ACM*, 15(1):11–15, January 1972. 16

[DLR77] A. P. Dempster, N. M. Laird, and D. B. Rubin. Maximum Likelihood from Incomplete Data via the EM Algorithm. *Journal of the Royal Statistical Society. Series B (Methodological)*, 39(1):1–38, 1977. 21

[FCC96] Ying-Lun Fok, J. C. K. Chan, and R. T. Chin. Automated analysis of nerve-cell images using active contour models. *Medical Imaging, IEEE Transactions on*, 15(3):353–368, June 1996. 22

[FGRdL09] G.M. Faustino, M. Gattass, S. Rehen, and C. de Lucena. Automatic embryonic stem cells detection and counting method in fluorescence microscopy images. In *Biomedical Imaging: From Nano to Macro, 2009. ISBI '09. IEEE International Symposium on*, pages 799 –802, 28 2009-july 1 2009. 22

[Fre61] H. Freeman. On the encoding of arbitrary geometric configurations. *Institute of Radio Engineers, trans. on Electronic Computers*, EC-10:260–268, 1961. 20

[FS88] T.L. Faber and E.M. Stokely. Orientation of 3d structures in medical images. *Pattern Analysis and Machine Intelligence, IEEE Transactions on*, 10(5):626–633, 1988. 12

[Gra72] G. Granlund. Fourier preprocessing for hand print character recognition. *IEEE Transactions on Computers*, C-21(2):195–201, 1972. 18, 31

[GW01] Rafael C. Gonzalez and Richard E. Woods. *Digital Image Processing.* Addison-Wesley Longman Publishing Co., Inc., Boston, MA, USA, 2nd edition, 2001. 9

[Har84] R.M. Haralick. Digital step edges from zero crossing of second directional derivatives. *Pattern Analysis and Machine Intelligence, IEEE Transactions on*, PAMI-6(1):58–68, 1984. 13

[HKB+11] Seungil Huh, D. F. E. Ker, R. Bise, Mei Chen, and T. Kanade. Automated Mitosis Detection of Stem Cell Populations in Phase-Contrast Microscopy Images. *IEEE Transactions on Medical Imaging*, 30(3):586–596, 2011. 22

[Hou59] P. V. C. Hough. Machine Analysis of Bubble Chamber Pictures. In *International Conference on High Energy Accelerators and Instrumentation*, CERN, 1959. 16

[HPH+11] C. Held, R. Palmisano, L. Haberle, M. Hensel, and T. Wittenberg. Comparison of parameter-adapted segmentation methods for fluorescence micrographs. *Cytometry A*, 79(11):933–45, 2011. 22

[Kap95] J. Kapuscinski. DAPI: a DNA-specific fluorescent probe. *Biotechnic & histochemistry*, 70(5):220–233, September 1995. 4

[KGBB11] Hui Kong, M. Gurcan, and K. Belkacem-Boussaid. Partitioning histopathological images: An integrated framework for supervised color-texture segmentation and cell splitting. *Medical Imaging, IEEE Transactions on*, 30(9):1661–1677, sept. 2011. 22

[KLW76] D.J. Ketcham, R.W. Lowe, and J.W. Weber. *Image Enhancement Techniques for Cockpit Displays.* Defense Technical Information Center, Hughes Aircraft, 1976. 10

[KMY+07] N. Kharma, H. Moghnieh, J. Yao, Y.P. Guo, A. Abu-Baker, J. Laganiere, G. Rouleau, and M. Cheriet. Automatic segmentation of cells from microscopic imagery using ellipse detection. *Image Processing, IET*, 1(1):39–47, march 2007. 22

[Koh88] Teuvo Kohonen. Neurocomputing: foundations of research. chapter Self-organized formation of topologically correct feature maps, pages 509–521. MIT Press, Cambridge, MA, USA, 1988. 21

[KY55] H. W. Kuhn and Bryn Yaw. The hungarian method for the assignment problem. *Naval Res. Logist. Quart*, pages 83–97, 1955. 38

[Lak06] J.R. Lakowicz. Introduction to fluorescence. In Joseph R. Lakowicz, editor, *Principles of Fluorescence Spectroscopy*, pages 1–26. Springer US, 2006. 3

[LCC01] Ping-Sung Liao, Tse-Sheng Chen, and Pau-Choo Chung. A Fast Algorithm for Multilevel Thresholding. *Journal of Information Science and Engineering*, 17:713–727, 2001. 23, 38

[LCC+13] B.L. Lopes, M. Coimbra, H. Castro, S. Romão, T. Cruz Cruz, and A.M. Tom'as. Cellnote: A framework for assisted annotation of cellular imaging. In *Conf. on Telecommunications - ConfTele*, May 2013. 37

[LFM+12] Pedro Leal, Luís Ferro, Marco Marques, Susana Romão, Tânia Cruz, Ana M. Tomá, Helena Castro, and Pedro Quelhas. Automatic assessment of leishmania infection indexes on in vitro macrophage cell cultures. In *Proceedings of the 9th international conference on Image Analysis and Recognition - Volume Part II*, ICIAR'12, pages 432–439, Berlin, Heidelberg, 2012. Springer-Verlag. 23, 41, 42

[Lin93] Tony Lindeberg. Detecting salient blob-like image structures and their scales with a scale-space primal sketch: a method for focus-of-attention. *Int. J. Comput. Vision*, 11(3):283–318, December 1993. 14

[Lin94] T. Lindeberg. *Scale-Space Theory in Computer Vision*. Kluwer Academic Publishers, 1994. 14, 23, 28

[Llo82] S. Lloyd. Least squares quantization in pcm. *Information Theory, IEEE Transactions on*, 28(2):129–137, 1982. 17

[Lop10] Bruno Lopes. Software Platform for Assisted Analysis of Cellular Images. Master's thesis, Department of Computer Science, University of Porto, 2010. 1, 7, 37

[LWBZ04] Joakim Lindblad, Carolina Wahlby, Ewert Bengtsson, and Alla Zaltsman. Image analysis for automatic segmentation of cytoplasms and classification of rac1 activation. *Cytometry Part A*, 57A(1):22–33, 2004. 22

[Mac67] J. B. Macqueen. Some methods of classification and analysis of multivariate observations. In *Proceedings of the Fifth Berkeley Symposium on Mathematical Statistics and Probability*, pages 281–297, 1967. 21

[MB90] F. Meyer and S. Beucher. Morphological segmentation. *Journal of Visual Communication and Image Representation*, 1(1):21 – 46, 1990. 17

[MFRS08] G. Martinez, J. G Frerichs, G. Rudolph, and T. Scheper. Three-dimensional cell counting for in-situ microscopy. In *Pattern Recognition, 2008. ICPR 2008. 19th International Conference on*, pages 1–4, 2008. 22

[MH80] D. Marr and E. Hildreth. Theory of edge detection. *Proceedings of the Royal Society of London. Series B. Biological Sciences*, 207(1167):187–217, 1980. 16

[NCPC13] João C. Neves, Helena Castro, Hugo Proença, and Miguel Coimbra. Automatic annotation of leishmania infections in fluorescence microscopy images. In *ICIAR*, pages 613–620, 2013. 51

[Nob79] Otsu Nobuyuki. A threshold selection method from gray-level histograms. *Systems, Man and Cybernetics, IEEE Transactions on*, 9(1):62 –66, jan. 1979. 12, 28

[Nog11] Pedro Nogueira. Determining Leishmania Infection Levels by Automatic Analysis of Microscopy Images. Master's thesis, Department of Computer Science, University of Porto, 2011. 23, 41, 42

[PA06] H. Proenca and L.A. Alexandre. Iris segmentation methodology for non-cooperative recognition. *Vision, Image and Signal Processing, IEE Proceedings* -, 153(2):199–205, 2006. 17

[PAA+87] Stephen M. Pizer, E. Philip Amburn, John D. Austin, Robert Cromartie, Ari Geselowitz, Trey Greer, Bart Ter Haar Romeny, and John B. Zimmerman. Adaptive histogram equalization and its variations. *Comput. Vision Graph. Image Process.*, 39(3):355–368, September 1987. 10

[Pre70] J. M. S. Prewitt. Object enhancement and extraction. *Picture Processing and Psychopictorics*, 1970. 13

[RHW86] D. E. Rumelhart, G. E. Hinton, and R. J. Williams. Learning internal representations by error propagation. *Mit Press Computational Models Of Cognition And Perception Series*, pages 318–362, 1986. 21

[Ser83] Jean Serra. *Image Analysis and Mathematical Morphology.* Academic Press, Inc., Orlando, FL, USA, 1983. 11

[SM06] Wang Shitong and Wang Min. A new detection algorithm (nda) based on fuzzy cellular neural networks for white blood cell detection. *Information Technology in Biomedicine, IEEE Transactions on*, 10(1):5–10, 2006. 22

[Soi03] Pierre Soille. *Morphological Image Analysis: Principles and Applications.* Springer-Verlag New York, Inc., Secaucus, NJ, USA, 2 edition, 2003. 11

[TUG02] N. Theera-Umpon and P.D. Gader. System-level training of neural networks for counting white blood cells. *Systems, Man, and Cybernetics, Part C: Applications and Reviews, IEEE Transactions on*, 32(1):48–53, 2002. 22

[Zei13] Carl Zeiss. Carl zeiss microscopy, May 2013. Available from: `http://microscopy.zeiss.com/microscopy/en_de/home.html`. 6, 28

Appendix A

Anexos

A.1 Interest measures obtained for each image

Image		#M	#P	#MI	PI	NPI	Infection Index
0000.zvi	ground truth	244	73	41	16.8 %	1.78	0.30
	prediction	233	58	41	17.6 %	1.41	0.25
0007.zvi	ground truth	239	132	59	24.7 %	2.24	0.55
	prediction	232	88	48	20.7 %	1.83	0.38
0029.zvi	ground truth	183	125	57	31.1 %	2.19	0.68
	prediction	180	78	50	27.8 %	1.56	0.43
0173.zvi	ground truth	156	188	74	47.4 %	2.54	1.21
	prediction	167	197	71	42.5 %	2.77	1.18
0362.zvi	ground truth	310	322	170	54.8 %	1.89	1.04
	prediction	303	197	134	44.2 %	1.47	0.65
0382.zvi	ground truth	369	255	146	39.6 %	1.75	0.69
	prediction	356	214	140	39.3 %	1.53	0.60
0424.zvi	ground truth	301	229	112	37.2 %	2.04	0.76
	prediction	286	141	92	32.2 %	1.53	0.49
0494.zvi	ground truth	450	681	298	66.2 %	2.29	1.51
	prediction	462	821	317	68.6 %	2.59	1.78
0565.zvi	ground truth	310	323	131	42.3 %	2.47	1.04
	prediction	307	340	154	50.2 %	2.21	1.11
0576.zvi	ground truth	281	367	126	44.8 %	2.91	1.31
	prediction	280	321	141	50.4 %	2.28	1.15
0618.zvi	ground truth	267	260	113	42.3 %	2.30	0.97
	prediction	265	252	121	45.7 %	2.08	0.95
0845.zvi	ground truth	221	172	84	38.0 %	2.05	0.78
	prediction	227	147	85	37.4 %	1.73	0.65

0880.zvi	ground truth	157	118	64	40.8 %	1.84	0.75
	prediction	155	114	60	38.7 %	1.90	0.74
0888.zvi	ground truth	230	106	63	27.4 %	1.68	0.46
	prediction	234	80	51	21.8 %	1.57	0.34
0939.zvi	ground truth	141	172	84	59.6 %	2.05	1.22
	prediction	143	174	83	58.0 %	2.10	1.22
1006.zvi	ground truth	214	241	104	48.6 %	2.32	1.13
	prediction	211	249	103	48.8 %	2.42	1.18
1014.zvi	ground truth	195	250	97	49.7 %	2.58	1.28
	prediction	196	272	107	54.6 %	2.54	1.39
1134.zvi	ground truth	291	22	22	7.6 %	1.00	0.08
	prediction	288	24	23	8.0 %	1.04	0.08
1275.zvi	ground truth	366	142	71	19.4 %	2.00	0.39
	prediction	359	104	67	18.7 %	1.55	0.29
1326.zvi	ground truth	191	195	86	45.0 %	2.27	1.02
	prediction	186	311	120	64.5 %	2.59	1.67
1444.zvi	ground truth	255	651	223	87.5 %	2.92	2.55
	prediction	249	683	208	83.5 %	3.28	2.74
1465.zvi	ground truth	192	387	160	83.3 %	2.42	2.02
	prediction	189	495	153	81.0 %	3.24	2.62
1477.zvi	ground truth	170	451	144	84.7 %	3.13	2.65
	prediction	165	454	136	82.4 %	3.34	2.75
1511.zvi	ground truth	194	71	37	19.1 %	1.92	0.37
	prediction	186	45	28	15.1 %	1.61	0.24

Table A.1: Comparison between the measures determined by manual and automatic analysis for each one of the 24 test images.

A.2 Precision, Recall and F-measure obtained for each image

Image	Macrophages						Parasites				
	TP	FP	FN	Precision	Recall		TP	FP	FN	Precision	Recall
0000.zvi	233	0	11	100.00 %	95.49 %		55	3	18	94.83 %	75.34 %
0007.zvi	231	1	8	99.57 %	96.65 %		87	1	45	98.86 %	65.91 %
0029.zvi	180	0	3	100.00 %	98.36 %		78	0	47	100.00 %	62.40 %
0173.zvi	152	15	4	91.02 %	97.44 %		154	43	34	78.17 %	81.92 %
0362.zvi	298	5	12	98.35 %	96.13 %		187	10	135	94.92 %	58.07 %
0382.zvi	352	4	17	98.88 %	95.39 %		189	25	66	88.32 %	74.12 %
0424.zvi	286	0	15	100.00 %	95.02 %		140	1	89	99.29 %	61.13 %
0494.zvi	435	27	15	94.16 %	96.67 %		645	176	36	78.56 %	94.71 %
0565.zvi	300	7	10	97.72 %	96.77 %		307	33	16	90.29 %	95.05 %
0576.zvi	276	4	5	98.57 %	98.22 %		305	16	62	95.02 %	83.11 %
0618.zvi	260	5	7	98.11 %	97.38 %		229	23	31	90.87 %	88.08 %
0845.zvi	221	6	0	97.36 %	100.00 %		128	19	44	87.08 %	74.42 %
0880.zvi	154	1	3	99.36 %	98.09 %		102	12	16	89.47 %	86.44 %
0888.zvi	227	7	3	97.01 %	98.70 %		75	5	31	93.75 %	70.75 %
0939.zvi	141	2	0	98.60 %	100.00 %		158	16	14	90.81 %	91.86 %
1006.zvi	208	3	6	98.58 %	97.20 %		233	16	8	93.57 %	96.68 %
1014.zvi	193	3	2	98.47 %	98.97 %		239	33	11	87.87 %	95.60 %
1134.zvi	280	8	11	97.22 %	96.22 %		19	5	3	79.17 %	86.36 %
1275.zvi	358	1	8	99.72 %	97.81 %		102	2	40	98.08 %	71.83 %
1326.zvi	185	1	6	99.46 %	96.86 %		174	137	21	55.95 %	89.23 %
1444.zvi	246	3	9	98.80 %	96.47 %		572	111	79	83.75 %	87.87 %
1465.zvi	189	0	3	100.00 %	98.44 %		364	131	23	73.53 %	94.06 %
1477.zvi	165	0	5	100.00 %	97.06 %		394	60	57	86.78 %	87.36 %
1511.zvi	185	1	9	99.46 %	95.36 %		42	3	29	93.33 %	59.16 %

Table A.2: The performance achieved for macrophage and parasite detection in each one of the 24 test images.

Appendix B

Automatic annotation of *Leishmania* infections in fluorescence microscopy images

Automatic annotation of *Leishmania* infections in fluorescence microscopy images

João C. Neves[1], Helena Castro[3], Hugo Proença[1], and Miguel Coimbra[2]

[1] Instituto de Telecomunicações, Universidade da Beira Interior, Faculdade de Engenharia, Departamento de Informática , Portugal
[2] Instituto de Telecomunicações, Faculdade de Ciências da Universidade do Porto, Portugal
[3] IBMC, Instituto de Biologia Molecular e Celular, Universidade do Porto , Portugal

Abstract. *Leishmania* is a unicellular parasite that infects mammals. Biologists are interested in determining the effect of drugs in *Leishmania* infections. This requires the manual annotation of the number of macrophages and parasites in images, in order to obtain the percentage of infection (PI), the average number of parasites per infected cell (NPI) and the infection index (IX). Considering that manual annotation is tedious, time-consuming and often erroneous, in this paper we propose an automatic method for automatic annotation of *Leishmania* infections using fluorescence microscopy. Moreover, when compared to related works, the proposed method is able to get superior performance under most perspectives.

Keywords: fluorescence microscopy, cell detection, cell counting, image segmentation

1 Introduction

The manual annotation of images is among the most tedious and time-consuming tasks that biologists often have to do. When attempting to automatize such process, due to data variability issues, it is usual to propose automatic methods for individual kinds of images, as those obtained from *Leishmania* infections using fluorescence microscopy. *Leishmania* is a unicellular parasite that infects mammals. Biologists are interested in determining the effect of drugs in this kind of infections infections. In order to infer conclusions from an experiment it is necessary to count the number of macrophages (mammals cells), the number of parasites and which are the parasites that are infecting each macrophage, to obtain the Percentage of Infection (PI), the mean Number of Parasites per Infected cell (NPI) and the Infection indeX (IX). In this type of images, fluorescence is used to mark the nucleus of the macrophages as red and blue and to mark the body of parasites as green. Moreover, the macrophages cytoplasm is also visible, which useful to determine the parasites that are infecting each macrophage. Figure 1 illustrates part of a fluorescence image, and the main components involved in the afore described process.

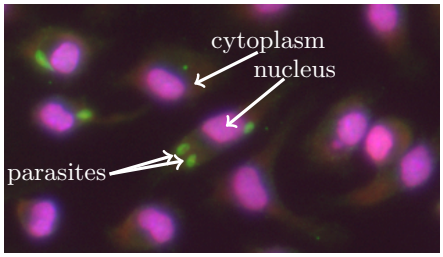

Fig. 1: Part of a fluorescence image and the most important structures involved in the annotation of *Leishmania* infections.

Considering that a limited number of research works focused in this problem, and that most of these methods lack of robustness, in this paper we present an approach to automatically annotate images obtained from *Leishmania* infections using fluorescence microscopy. As our experiments confirm, the main contribution is the increase of the effectiveness of the resulting automated systems, and of its robustness handling the high variability of shapes and textures that often appear in this type of images.

The remaining of this paper is organized as follows: section 2 overviews the most relevant works in the scope of our method. Section 3 describes the proposed strategy and section 4 discusses the observed performance, when compared to other techniques. Finally, conclusions are drawn in section 5.

2 Related Work

The automatic processing of cellular data has been the scope of several research works, even though the specificities of fluorescence microscopy data were considered in a reduced number of methods. In [1], authors counted the number of axons in nerve cells based on active contours. Kharma *et* al performed an automatic segmentation of cells on microscopy images [2]. Two main phases are described. The first aims at extracting the cells from the background combining an adaptive threshold with morphological operators. The second phase separates the overlapping cells supposing that the general shape of cells is an ellipsis. In [3] a method was proposed to detect and count stem cells in fluorescence images.

Due to data specificities, the above described methods cannot be used in the kind of images we aim at. To the best of our knowledge, the automatic annotation of *Leishmania* infections using fluorescence microscopy were only addressed in two different approaches. The first was proposed by Nogueira *et* al. [4] where the detection of the macrophages and parasites was carried out by adaptive threshold techniques [5]. Each region detected is a cluster of k nucleus or parasites that occur due to the overlapping of objects. Features as the area and the center of mass are extracted from the region presuming that they can

be discriminant in what concerns the number of objects present. A machine learning approach predicts the value of k for each region given a set of features. A support vector machine (SVM) was trained for this task along with a rule-based statistical classifier. A voting system was then used to conciliate the predictions of the classifiers and thus output the value of k predicted for a region. At last, each region was de-clustered with Gaussian Mixture Models (GMM) using k mixtures. The second approach was developed by P.Leal *et* al's [6]. Authors used the Difference of Gaussians (DoG) filter to enhance objects at the desired scale, before detecting the macrophages nuclei and parasites. An iterative process combined with an adaptive threshold method was used, in order to tune the value of standard deviation of DoG to the scales of macrophages nuclei/parasites present in the image. Next, the blue and green channel were filtered to obtain the locations of macrophages nuclei and parasites, respectively. These locations were used not only as the result of automatic annotation but also as seeds to the watershed algorithm. The watershed algorithm segments the cytoplasm of the macrophages, so that a more accurate association between macrophages and parasites can be achieved.

3 Proposed Method

A cohesive perspective of the main steps of our method are given in Figure 2. Even though our explanation will be oriented to the macrophages, the parasites are processed in a much similar the same way, with exception of the color channel used (red in the case of parasites).

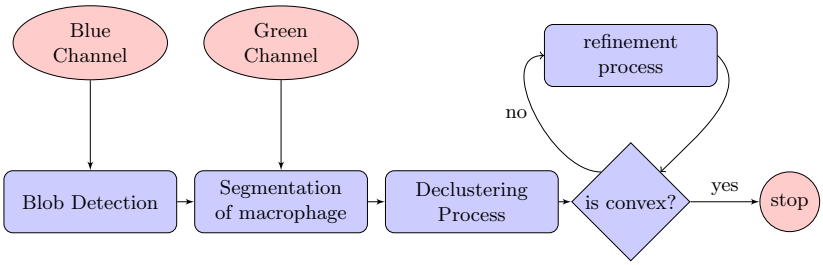

Fig. 2: Flowchart containing the main steps of our method.

The process starts by detecting a set of blobs, aiming to coarsely find the locations of the macrophages. Assuming that their typical shape is circular, we used the scale-space theory proposed by Lindberg [7] with slight modifications. In [8] it is shown that a Laplacian of Gaussian (LoG) filter, with standard deviation σ, is able to detect bright circular objects, known as blobs, with radius $\sqrt{2}\sigma$ by searching the local maximum of $SS(r, x, y)$

$$SS(r,x,y) = \frac{r^2}{2} LoG(\frac{r}{\sqrt{2}}, x, y) * I(x,y), \quad (1)$$

where r is the radius of blobs to detect in the image I. Even though originally a neighbourhood of [x,y,r]=[3,3,3] is used to find local maximums of SS, we used [x,y,r]=[3,3,∞], i.e., we searched over all possible radii, in order to avoid the detection of blobs of different sizes at the same location. Figure 3a illustrates the results of the blob detection phase.

Once the locations of the blobs are determined, a Region of Interest (ROI) is gathered from the green channel centered at the blob location with dimensions $4r$ x $4r$. These values should be large enough to enclose the cytoplasm of the macrophage. In each region the K-means algorithm is used to map each instance (pixel) to one cluster, by feeding it with the pixels intensity and the values of a two dimensional Gaussian function centered at the blob location. Figure 3b illustrates the results of clustering applied to a ROI. Since, the parasites and the macrophages cytoplasm are typically brighter than the background, we select the two clusters with highest mean luminance. This results in a binary image in which the morphological erosion and dilation are applied intercalated with the removal of all the connected components that are not linked to blob location, yielding a binary mask, designated hereinafter as B, that should contain the cytoplasm area of the detected blob. Figure 3c illustrates an example of the binary mask obtained from the clustered region given in Figure 3b.

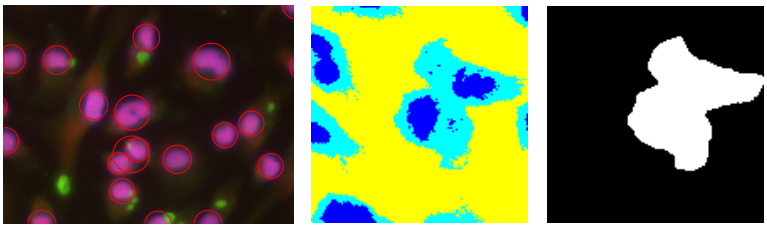

(a) Blob detection results. (b) K-means output (c) Binary Mask

Fig. 3: Results obtained from different phases of our method.

Having B, it is necessary to separate the cytoplasm associated with the detected blob from other overlapping cytoplasms. The rationale behind this step is based in the concave points of the shape contour in the binary mask, which is parametrically given by:

$$C(t) = (x(t), y(t)), t \in \{0, 1, ..., L\}, \quad (2)$$

where L is the length of the contour. A point $C(k)$ is concave if:

$$\|\overrightarrow{C(k-1)C(k)} \times \overrightarrow{C(k-1)C(k+1)}\| < 0. \quad (3)$$

Considering that $C(t)$ is a discrete contour, it has a lot of details that must not be identified as concave points. Due to this, we used the elliptic Fourier descriptors [9] to smooth the contour by removing the high frequencies of $C(t)$. The contour is further reconstructed using only the lowest frequencies:

$$\begin{aligned} x_s(t) &= a_0 + \sum_{n=1}^{N} a_n cos(\frac{2\pi.nt}{L}) + b_n sin(\frac{2\pi.nt}{L}), \\ y_s(t) &= c_0 + \sum_{n=1}^{N} c_n cos(\frac{2\pi.nt}{L}) + d_n sin(\frac{2\pi.nt}{L}). \end{aligned} \tag{4}$$

We used $N = \frac{L}{f}$ to obtain the smoothed contour $C_s(t) = (x_s(t), y_s(t))$. f is a parameter that controls the number of frequencies selected according to the size of the contour ($f = 15$ in our case). Next, regions of connected concave points are constructed, and from each region are retrieved three points. These points, $\{P_{1i}, P_{2i}, P_{3i}\}$, are the initial point, the point with highest curvature and the final point that are used to obtain the features of the i_{th} region. The concavity angle of i^{th} region is defined by $\psi(i) = \angle P_1 P_2 P_3$ and the director vector is given by $\overrightarrow{v}(i) = \overrightarrow{P_1P_2} + \overrightarrow{P_3P_2}$. In the majority of the cases the shape of two overlapping cytoplasms has a pair of concave regions. Figure 4 illustrates (in green) the smoothed contour of the shape given in Figure 3c. The smoothed contour presents the two concave regions originated by the intersection of cytoplasms, designated as true concavities, amongst other concave regions, designated as false concavities. Hence, it is necessary to find the set of regions more likely to be true concavities and then match them. We solved the first issue by considering regions that satisfy $\psi(i) < \frac{11\pi}{12}$, discarding regions of weak concavity. Figure 4 illustrates (in red) the concave regions of $C_s(i)$ after filtering. We also propose a score method to match regions using their concavity and the angle formed by vector $\overrightarrow{P_{2i}P_{2j}}$ and $\overrightarrow{v}(i)$, designated hereinafter as $\alpha(i,j)$. $\alpha(i,j)$ is used to determine if two regions must be matched, since $\alpha(i,j) \to 0$ when the i^{th} region must be matched to the j^{th} region. The score to match the i^{th} region to the j^{th} region is given by

$$M(i,j) = w_1 \frac{\alpha(i,j)}{\pi} + w_2 \frac{\psi(i,j)}{\pi} + w_3 \frac{d(i,j)}{max(d)}, \tag{5}$$

and the cost of the complete match is given by

$$\kappa(i,j) = \frac{M(i,j) + M(j,i)}{2}, \tag{6}$$

where $W = \begin{bmatrix} w_1 & w_2 & w_3 \end{bmatrix}$ is the set of weights that controls the importance of each region feature. In our approach we used $W = \begin{bmatrix} 0.5 & 0.4 & 0.1 \end{bmatrix}$, as the angle $\alpha(i,j)$ and the concavity sharpness were considered the most important factors. The distance between two regions, $d(i,j)$, is used to favor closest regions.

Due to $M(i,j)$ definition, it can be derived that $\kappa \in [0,1]$. The best match between regions is given by the minimums in $\kappa(i,j)$. Instead of determining the

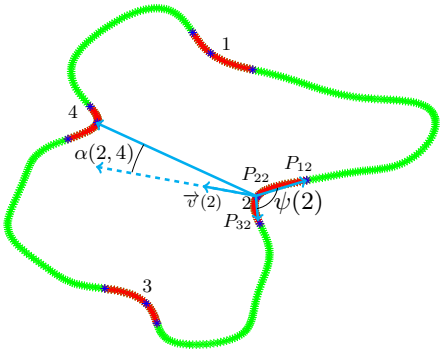

Fig. 4: The smoothed contour extracted from the binary mask in Figure 3c. In red are presented the four concave regions of $C_s(t)$. The features of the second region are also presented.

region	1	2	3	4
1	-	0.47	0.62	0.58
2	-	-	0.56	0.36
3	-	-	-	0.41
4	-	-	-	-

Table 1: Example of the cost $\kappa(i,j)$ involved in the point matching process.

set of pairs that minimizes the sum of κ, we determine the set of pairs iteratively, by finding the absolute minimum in $\kappa(i,j)$, among the non-matched regions up to $\kappa(i,j) < 0.6$. Table 1 gives the values of $\kappa(i,j)$ for the example in Figure 4. Here, the first pair chosen was $(2,4)$ and the second $(1,3)$, since there are no other options available. As $\kappa(1,3) > 0.6$ this pair is not matched.

Having observed slight inaccuracies in the outputs of the previously described phases, we finally aimed at a refinement process, in order to determine if the cytoplasm segmentation is complete or not, removing the surplus parts in the former case. As in the majority of the cases the cytoplasm shape is convex, we used the convexity of the shape presented in B. The contour of B is extracted and smoothed using $\frac{L}{2f}$ frequencies. $C_s(i)$ is considered convex if $\psi(i) > \frac{11\pi}{12}$ for all the concave regions in $C_s(i)$. Next, we allow a more flexible definition of convex shape by lowering the threshold, and also a more flexible matching between the concave regions. Also, we forced cell separation when only one concave point exists.

4 Results and Discussion

The performance of our method was compared to the approach of Leal *et* al. [6], as we observed that this was the outperforming method for the kind of images we used. Ten images were used, which was not considered a small number, as they contain over 3 000 macrophages and 3 250 parasites. Images were annotated

	Our method			Leal *et* al. method [6]		
	Precision(%)	Recall(%)	F-measure(%)	Precision(%)	Recall(%)	F-measure(%)
Macrophages	98.6	96.5	97.5	97.4	99.4	98.4
Parasites	86.8	87.1	86.9	77.8	79.9	78.8

Table 2: Summary of the results obtained for our method, when compared to the values yielded by Leal *et* al. [6] approach.

by biologists and cross-verified. Figure 5a illustrates the results obtained by our method: the contours of the cytoplasm of each macrophage were delimited with different colors. In Figure 5b, similar results due to Leal *et* al. method are given: the black points represent the center of each detected macrophage. Also, Table 2 summarizes the performance levels obtained by both methods.

The main difference between the performance of both methods is highlighted in the cells marked as 1 and 2. Our method is able to overcome the problem associated with multiple nuclei in a macrophage. In spite of blob detection phase recognize two nuclei in each region, the segmentation of the cytoplasm performed in our approach is able to decide if they belong to same macrophage. This improvement leads to a lower number of false positives, and thus increases the precision of our method. This justifies why our method has a slightly higher precision than the other method. On the other hand, our method is outpaced in recall due to the rejection of shapes that are not convex after applying the refinement process. In what concerns the parasite detection, our method has outpaced Leal *et* al.'s method. The higher precision in parasite detection can be explained also by our segmentation phase that decreases the false positive rate, whereas the higher recall can be explained mainly by our parasite nuclei detection using red channel, that can discover parasites that would not be able to identify using only the green channel.

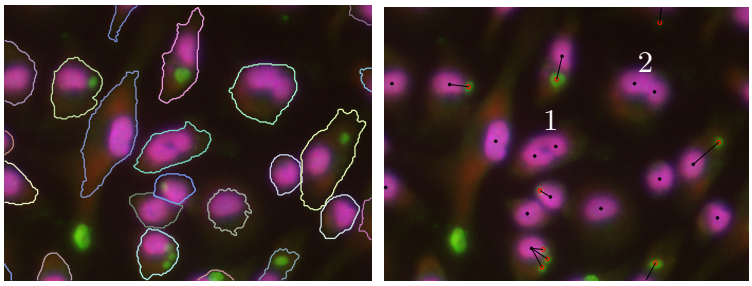

(a) (b)

Fig. 5: Example of the results obtained for a single image.

5 Conclusion

We described a new method to automatically annotate images with *Leishmania* infections and the results yielded were compared to the approach of Leal *et* al. [6], observed to be the one that outperforms in this kind of data. We concluded that the proposed method is able to obtain similar performance to Leal et al. in the case of macrophages and far better performance in the case of parasites. Also, we would like to highlight the modularity of our approach, which can be easily adapted to other types of cellular images. The blob detection phase can be useful to detect nuclei or cells in many type of cellular images, as the most common shape of cells is circular. Besides, our separation method has a broader application, as it can be used to separate overlapping objects in other type of problems and other type of microscope images.

Acknowledgments. The financial support given by "IT-Instituto de Telecomunicações" in the scope of the IT/LA/1086/2011 research project "CellNote Touch: Touch-based Interactive Annotation of Cellular Images" and the source code of Leal *et* al. method [6] provided by the authors is acknowledged.

References

1. Fok, Y.L., Chan, J.C.K., Chin, R.T.: Automated analysis of nerve-cell images using active contour models. Medical Imaging, IEEE Transactions on **15**(3) (June 1996) 353–368
2. Kharma, N., Moghnieh, H., Yao, J., Guo, Y., Abu-Baker, A., Laganiere, J., Rouleau, G., Cheriet, M.: Automatic segmentation of cells from microscopic imagery using ellipse detection. Image Processing, IET **1**(1) (march 2007) 39–47
3. Faustino, G., Gattass, M., Rehen, S., de Lucena, C.: Automatic embryonic stem cells detection and counting method in fluorescence microscopy images. In: Biomedical Imaging: From Nano to Macro, 2009. ISBI '09. IEEE International Symposium on. (28 2009-july 1 2009) 799 –802
4. Nogueira, P.: Determining Leishmania Infection Levels by Automatic Analysis of Microscopy Images. Master's thesis, Department of Computer Science, University of Porto (2011)
5. Nobuyuki, O.: A threshold selection method from gray-level histograms. Systems, Man and Cybernetics, IEEE Transactions on **9**(1) (jan. 1979) 62 –66
6. Leal, P., Ferro, L., Marques, M., Romão, S., Cruz, T., Tomás, A.M., Castro, H., Quelhas, P.: Automatic assessment of leishmania infection indexes on in vitro macrophage cell cultures. In: Proceedings of the 9th international conference on Image Analysis and Recognition - Volume Part II. ICIAR'12, Berlin, Heidelberg, Springer-Verlag (2012) 432–439
7. Lindeberg, T.: Scale-Space Theory in Computer Vision. Kluwer Academic Publishers (1994)
8. Lindeberg, T.: Detecting salient blob-like image structures and their scales with a scale-space primal sketch: a method for focus-of-attention. Int. J. Comput. Vision **11**(3) (December 1993) 283–318
9. Granlund, G.: Fourier preprocessing for hand print character recognition. IEEE Transactions on Computers **C-21**(2) (1972) 195–201